Remote sensing of optical and microphysical properties of cirrus clouds using MODIS channels: methodology and sensitivity to physical assumptions

P. Rolland and K. N. Liou
Department of Atmospheric Sciences
University of California, Los Angeles, CA

M. D. King and S. C. Tsay
Goddard Space Flight Center, Greenbelt, MD

G. M. McFarquhar
National Center for Atmospheric Research, Boulder, CO

Submitted to the Journal of Geophysical Research

Abstract. A methodology for the detection of cirrus clouds and the retrieval of their microphysical and optical properties based on observations of reflected sunlight is introduced. The retrieval method is based on correlation of the bidirectional reflectance of three channels, 0.65, 1.6, and 2.2 μm, that are available on board Earth Observing System (EOS) Moderate Resolution Imaging Spectroradiometer (MODIS). Validation studies using microphysical measurements and MODIS Airborne Simulator (MAS) observations illustrate the nature of the potential errors associated with the retrieved optical depth and mean effective ice crystal size. The effects of the physical assumptions involving ice crystal size distribution and shape employed in the algorithm are subsequently assessed. In terms of the microphysical models used for radiation calculations, the ice crystal shape assumption is found to have the most significant impact on the retrieved parameters. The effect of the background surface reflectance on the retrieval results is further examined and we show that in order to reliably infer thin cirrus parameters from solar reflectance measurements, it is essential to properly account for the background radiation both over land and ocean surfaces. Finally, we present the measured ice microphysical data for tropical cirrus as a function of cloud development and ambient temperature to illustrate the importance of vertical inhomogeneity for validation studies.

Introduction

In view of the physical location and the complex nature of their optical and physical properties, cirrus clouds have been identified as one of the major unsolved components in weather and climate research [*Liou*, 1986; 1992]. The influence of cirrus clouds on the radiation field of the earth-atmosphere system depends on the solar and thermal IR radiative properties, referred to as the greenhouse vs albedo effect, which in turn are modulated by the cloud composition and physical location in the atmosphere. Thus, in order to quantify the radiative effects of cirrus, microphysical (ice crystal size distribution and shape), structure (height and spatial extent), and optical (optical depth) properties are required. A realistic treatment of cirrus cloud physical and radiative properties is essential to achieve physically based climate modeling and predictions. Satellite remote sensing methods must be developed and validated to provide the required cirrus cloud parameters on a global scale, in conjunction with GCM and climate modeling development.

A number of approaches based on the principles of radiative transfer have been developed to infer cloud optical depth and mean effective ice crystal size from satellites. They can be divided into two groups, with some overlap: reflection and emission techniques. The former relies on the reflectance characteristics of solar wavelengths, implying day-time use, while the latter uses radiation emitted in the thermal IR spectrum, and is thus applicable to night as well as day conditions. Pure IR methods are based on the variation of cloud emittance as a function of wavelength. *Liou* [1974] demonstrated that the optical properties of cirrus varied between 11 and 12 μm. *Inoue* [1985] developed a method using the brightness temperature difference between 11 and 12 μm to determine the infrared emissivity of cirrus clouds by assuming an implicit mean particle size. *Liou et al.* [1990] developed an iterative technique to infer cirrus temperature and optical depth from 6.5 and 11 μm radiances. *Ackerman et al.* [1990] introduced a method to estimate cirrus cloud particle size in terms of ice-sphere effective radius by fitting the observed variations in equivalent blackbody temperature to theoretical calculations of absorption coefficients for four infrared wavelengths. *Ou et al.* [1993] developed a method to infer cirrus optical depth, mean effective ice crystal size, and temperature from night-time 3.7 and 10.9 μm radiances, based on the dependence of cloud particle size on temperature. Subsequent modification of this method for day-time radiances was carried out by *Rao et al*. [1995], by numerically removing the solar component of

the 3.7 μm radiance. *Ou et al.* [1995] applied their removal-retrieval technique [*Ou et al.* 1993; *Rao et al.* 1995] to AVHRR data collected during FIRE I and II, and carried out a validation study using collocated *in situ* ice crystal size distributions obtained from optical array two-dimensional cloud probes (2-DC) data and ground-based lidar return imageries. They demonstrated that the retrieved cirrus cloud temperature, mean effective ice crystal size, and optical depth closely matched the observed values.

Solar reflection methods are based on the fact that reflection of clouds at a non-absorbing channel in the visible spectrum is primarily a function of the cloud optical depth, whereas reflection at a water (or ice) absorbing channel in the near IR is primarily a function of cloud particle size [e.g., *King et al.,* 1997]. One of the earliest applications of the reflection method was demonstrated by *Hansen and Pollack* [1970] who, using theoretical computations, attempted to explain the spectral variations in aircraft reflectivity measurements [*Blau et al.,* 1966] in terms of particle phase and size. *Twomey and Seton* [1980] theoretically showed that the mean droplet radius and optical depth can be determined for optically thick clouds from simultaneous reflectance measurements in the visible and near IR. Applications of this multispectral correlation technique using 0.75, 1.0, 1.2, and 2.25 μm aircraft reflectance measurements were relatively unsuccessful [*Twomey and Cocks,* 1982]. However, improvement was made with the help of a modernized radiometer and the addition of the 1.66 μm wavelength [*Twomey and Cocks,* 1989]. *Nakajima and King* [1990] showed that a tri-spectral approach (0.75, 1.6, and 2.2 μm) can be used to simultaneously retrieve the optical depth and mean effective particle size of water clouds, and that the addition of a third channel was desirable in order to remove ambiguities arising from the monochromatic variation of size and single-scattering albedo. They also found that the retrieved value of effective particle size corresponds to some upper portion of the cloud, implying the necessity to make some adjustment in order to estimate the mean effective particle size representative of the entire cloud. Later analysis of the aircraft observations at 0.75, 1.65, and 2.16 μm [*Nakajima et al.,* 1991] over stratocumulus clouds produced excellent correlation between the remotely-sensed, center-adjusted effective radii and *in situ* observations. *Wielicki et al.* [1990] estimated particle sizes for water and ice clouds from Landsat observations at 0.83, 1.65, and 2.21 μm. Good agreement was found between observed and retrieved effective sizes for water clouds, but very large discrepancies existed for ice clouds. The major problems involving ice clouds are associated with uncertainty in the scattering and absorption properties of

nonspherical particles [e.g., *Wielicki et al*, 1995; *Liou*, 1986]. Further theoretical and observational works are needed for ice clouds.

In this paper, we present a cirrus remote sensing methodology using spectral radiation measurements in the solar region (0.6, 1.6, and 2.2 μm) along with the results of validation studies. The validation studies are carried out using MODIS Airborne Simulator (MAS) observations, 2-DC and Video Ice Particle Sampler (VIPS) data, collected as part of the Central Equatorial Pacific Experiment (CEPEX) and the Subsonic Aircraft: Contrail and Cloud Effects Special Study (SUCCESS). Further, an error analysis is carried out by means of a series of sensitivity studies to investigate the limitations of the retrieval technique in terms of the various assumptions inherent to the method. Specifically, the effects of the ice crystal size distribution and shape, variance of the underlying surface reflectance, and vertical cloud inhomogeneity assumptions are investigated.

2. Retrieval Method

The MAS instrument [*King et al*., 1996] has provided well-calibrated high-resolution spectral radiation measurements at 50 wavelengths during the course of a number of field experiments. Some of these campaigns specifically targeted cirrus clouds, providing concurrent measurements of cloud microphysics and radiation. The development of an algorithm for the retrieval of cirrus optical depth and mean effective ice crystal size using the MAS channels radiance involves a series of processing steps. Microphysical data must be analyzed in order to characterize the size and shape of ice crystals observed in cirrus clouds. Calculations of absorption/scattering effects by ice crystals are then carried out on the basis of this analysis. These calculations provide the parameters necessary to simulate, using a radiative transfer program, the reflectance and transmittance properties of cirrus clouds. Theoretical values of cloud reflectance thus generated for arrays of known optical depths and effective sizes can then be interpolated and statistically fitted to observed values. These steps constitute the basis for the retrieval algorithm and are described in this section.

We have undertaken the construction of lookup tables of combined cirrus and underlying surface bidirectional reflectance. In order to calculate reflectance values for various cirrus conditions, representative size and shape distributions for various cloud types considered must be defined. The

microphysical properties of midlatitude cirrus are better documented [e.g., *Heymsfield and Platt,* 1984]. However, understanding the intricate microphysics involving tropical cirrus anvils is a subject of current research. In conjunction with remote sensing applications, we have analyzed *in situ* observations of anvils sampled during CEPEX, which was conducted to understand the relative role of tropical cirrus anvils in the radiative and dynamic equilibrium of the tropical atmosphere. In this experiment, the Particle Measuring Systems (PMS) 2-DC measured ice crystals ranging from 30 to 3000 μm in maximum dimension with a resolution of 30 μm, while the VIPS was used to identify ice crystals too small to be detected by the 2-DC [*McFarquhar and Heymsfield*, 1996]. Three collection days, March 16, April 1, and April 4, 1993, were selected from the CEPEX database because of the availability of collocated microphysical and radiative data, and because of their variety of meteorological situations, including anvils associated with developing, mature, and dissipating cumulonimbus systems. For the purpose of this study, six representative size distributions spanning a mean effective ice crystal size range of 21 to 91 μm were selected from the CEPEX analysis. For midlatitude cirrus, six size distributions described by *Rao et al.* [1995], spanning a mean effective ice crystal size range of 23 to 123 μm, were used. Ice crystal habits were determined using maximum dimension and area ratio, the ratio of the ice crystal projected area to the area of a circle having a diameter equal to maximum dimension, based on a number of microphysical studies [*Heymsfield and Knollenberg*, 1972; *Mitchell et al.*, 1990; *Personne et al*., 1991; *Iaquinta and Personne*, 1992], and a classification scheme that has been previously used at NCAR to classify particle shape [*McFarquhar et al.*, 1999]. The four habits considered in this study are plates, columns, bullet rosettes, and large column aggregates.

After selecting an array of representative size distributions, we need to obtain reliable single-scattering properties and phase functions for each type of ice crystals in terms of size and shape for remote sensing applications. The scattering of light by spheres can be solved by the exact Lorenz-Mie theory. An exact solution for the scattering of light by nonspherical ice crystals and aerosols, however, does not exist for all sizes and shapes observed in the earth's atmosphere. In recent years, *Takano and Liou* [1989a, 1995] and *Liou and Takano* [1994] developed a light scattering program allowing the computation of scattering, absorption, and polarization properties of plates, columns, bullet rosettes, aggregates and dendrites for use in radiation/climate modeling and remote sensing applications. This program is based on the

geometric ray-tracing approach, which utilizes the localization principle for light rays, the Fresnel reflection and refraction law, and the equal partition of diffraction and Fresnel rays. In order to circumvent limitations inherent in the ray tracing approach with respect to applicable size parameter, *Yang and Liou* [1996] developed an improved methodology for geometric ray tracing. Mapping of the electric field at the particle surface, determined from the Fresnel law, to the far field is carried out based on the exact electromagnetic wave theory, thus fully accounting for the phase interferences. This method can be adequately applied to size parameters as small as 15. We have used the improved geometric ray tracing method for light scattering to develop a database of the single-scattering parameters for the four ice crystal habits noted above and 44 size bins ranging from 10 to 2700 μm for the 0.65, 1.6, and 2.2 μm wavelengths. These parameters include the phase function, the single-scattering albedo, the extinction cross-section, and the asymetry parameter.

In order to compute the theoretical bidirectional reflectance, the single-scattering properties corresponding to a pre-determined ice crystal size and shape distribution must be known *a priori*. The bidirectional reflectance is defined as follows:

$$R(\mu,\phi;\mu_0,\phi_0) = \pi I(0,\mu,\phi) / (\mu_0 F_0), \tag{1}$$

where μ is the cosine of the zenith angle, ϕ the corresponding azimuthal angle, the subscript 0 refers to values associated with the positioning of the sun, F_0 is the solar irradiance, and $I(0, \mu, \phi)$ is the upwelling radiance at the top of the atmosphere. The scattering properties for a given ice crystal distribution are calculated by integration of the various scattering parameters over the numbers of sizes and shapes determined from observations. For example, the phase function for a sample of ice crystals is defined by

$$\overline{P(\Theta)} = \frac{\sum_i \int_{L_{\min}}^{L_{\max}} \sigma_{s,i}(L) P_i(\Theta, L) n_i(L) dL}{\sum_i \int_{L_{\min}}^{L_{\max}} \sigma_{s,i}(L) n_i(L) dL}, \tag{2}$$

where the summation i extends over the various ice crystal habits in a given distribution, σ_s is the scattering cross section, and $n(L)$ is the observed number concentration for maximum dimension L. The scattering and extinction cross sections, the single-scattering albedo, and the asymetry factor are

obtained in a similar manner. Moreover, to represent the ice crystal size distribution, the mean effective ice crystal size is defined as follows:

$$D_e = \frac{\sum_i \int_{L_{\min}}^{L_{\max}} V_i n_i(L) dL}{\sum_i \int_{L_{\min}}^{L_{\max}} A_i n_i(L) dL}, \tag{3}$$

where V is the volume of an ice crystal and A is the geometric projected area of an ice crystal on a surface perpendicular to the incident light beam. In this manner, the shape of irregular ice crystals is accounted for in this definition.

For multiple scattering contributions, we followed the adding/doubling method for radiative transfer [*Takano and Liou,* 1989b]. This method includes full Stokes parameters for the transfer of monochromatic radiation in an inhomogeneous atmosphere that is predivided into a number of appropriate homogeneous layers. The single-scattering parameters derived for the size/shape distributions are incorporated in multiple-scattering computations, which use the similarity principle for radiative transfer to account for the diffraction peak and δ-forward transmission produced by hexagonal ice particles.

Once the single-scattering and radiative transfer computations have been accomplished, the next step in retrieving the properties of cirrus clouds is the detection of cirrus pixels, based on a series of threshold tests. First, a visible radiance (0.65 μm) threshold is applied. Pixels with high visible reflectance are classified as cloudy, and pixels with low visible reflectance undergo further tests for thin cirrus cases. These tests include a brightness temperature (BT) difference between the 11 and 12 μm channels, and a 1.9 μm threshold test. The first test is based on the fact that thin cirrus display a spectral variation of BT over the atmospheric window region [*Inoue,* 1985]. The second test uses the fact that cirrus are located above 90-99% of the tropospheric water vapor [e.g., *Liou,* 1986] so that solar radiation at a strong H_2O band is almost entirely absorbed in the lower troposphere. Thus, the 1.9 μm channel receives little scattered radiance from the surface and/or low clouds and the atmosphere below them. Consequently, the cirrus signal stands out by comparison. For pixels classified as cloudy by the initial test, a BT

threshold (11 μm) test and a 1.9 μm reflectance threshold test are applied to separate low clouds from cirrus. Note that the aforementioned channels are a part of the MAS instrument.

The retrieval scheme begins with the construction of lookup tables that contain a combined surface/cloud bidirectional reflectance corresponding to various mean effective ice crystal sizes and optical depths for a number of relevant geometrical configurations. The bidirectional reflectance for cirrus over a Lambertian surface can be computed using the parametric equation in the form [*Liou,* 1980]

$$R_i(\mu_0, \mu, \Delta\phi) = r_i(\mu_0, \mu, \Delta\phi) + \frac{T_i(\mu_0)T_i(\mu)r_{cl,i}}{1 - r_{cl,i}\alpha_{c,i}}, \tag{4}$$

where r_{cl} is the cloud-base reflectance, and the subscript i refers to the three channels used in the retrieval (0.65, 1.6, and 2.2 μm). The adding/doubling program for radiative transfer described above calculates the cloud layer bidirectional reflectance $r(\mu_0, \mu, \Delta\phi)$, transmittances $T(\mu)$ and $T(\mu_0)$, and albedo α_c (i.e., hemispherical reflectance) corresponding to the viewing geometry parameters (solar zenith angle θ_0, radiometer scan zenith angle θ, and relative azimuthal angle $\Delta\phi$). The first term in Eq. (4) represents the portion of the incident energy directly reflected by the cloud towards the sensor, while the second term represents the contribution of energy reflected to the sensor from multiple reflections between the cloud and the surface. The cloud base reflectances , r_{cl}, for the three channels used in the retrieval are obtained by using a clear pixel statistical scheme applied for every 300 scanlines. A histogram of cloud base reflectance is constructed for each of the three channels, using the pixels flagged as clear. The mode of the histogram is selected as the cloud base radiance, equivalent to the corrected surface reflectance including the atmospheric contribution below cirrus [e.g., *Liou et al.,* 1990]. Upon selecting r_{cl}, theoretical values of the cirrus bidirectional reflectance over a scene considered are generated using Eq. (4).

Bidirectional reflectance calculations are computationally expensive. Furthermore, each MAS image presents a number of scan angles (85° full swath aperture), solar angles, and relative azimuthal angles (depending on the motion of the aircraft). Thus, in order to perform the retrieval with a reasonable degree of precision, the lookup tables, which are computed typically for eight optical depths from 0.1 to 16 and six mean effective ice crystal sizes, must be interpolated from the relatively crude grid to a higher

resolution of 1 μm for size and 0.25 for optical depth to process a MAS image. The interpolation technique used for this study is a bi-cubic spline, where a series of cubic splines are used to interpolate a two-dimensional plane [*Cline*, 1974]. The interpolation procedure must be carried out for every viewing geometry pertinent to a MAS file being processed which typically involves 33 scan-angle bins at 2.5° resolution for an 85° scan width.

From values of the theoretical cloud reflectance obtained in this manner, an optimal fit with the observed cloud reflectance values is then carried out. Maximizing the probability that the measured reflectances $R_m(\mu_0, \mu, \Delta\phi)$ have the functional form $R_c(\tau, D_e, \mu_0, \mu, \Delta\phi)$ is equivalent to minimizing the χ^2 statistical formulation [*Nakajima and King,* 1990], defined as

$$\chi^2 = \sum_i [\ln R_m^i(\mu_0, \mu, \Delta\phi) - \ln R_c^i(\tau, D_e, \mu_0, \mu, \Delta\phi)]^2, \tag{5}$$

where the summation extends over the three channels, and the subscripts *m* and *c* refer to measured and calculated reflectances, respectively. The functional form of the bidirectional reflectance thus obtained simultaneously provides the retrieved values of cloud optical depth (visible) and effective mean ice crystal size. This retrieval procedure is performed on a pixel-by-pixel basis.

For validation, we used the collocated ice crystal size distributions collected by the 2-DC optical probe. This probe provided measurements of the number concentration, maximum dimension (L), and area ratio (AR). From the six second averaged quantities, the mean effective ice crystal size can be obtained using the following relationships:

$$D_e = \frac{IWC}{\rho_i A_c}, \tag{6}$$

$$IWC = \int_{L_{\min}}^{L_{\max}} V \rho_i n(L) dL, \tag{7}$$

$$A_c = \frac{\pi}{4} \sum_i \sum_j n(D_i, AR_j) AR_j D_i^2, \tag{8}$$

where ρ_i is the density of ice, A_c is the total cross sectional area per unit volume, V is the volume calculated using the *Auer and Veal* [1970] relationships, and the subscripts i and j refer to summations

over the size and area ratio bins, respectively. Finally, the visible optical depth can be obtained from the product of the extinction coefficient and the observed cloud geometric depth.

In Fig. 1a, the retrieved cirrus optical depth and mean effective ice crystal size are compared with those derived from the analysis of concurrent *in situ* microphysical observations. Also shown for illustration of the collocation process are examples of the visible imageries overlaid with aircraft paths and 2-DC data measurement locations (Fig. 1b). Radiation and microphysical measurements carried out during CEPEX, specifically during the course of tracks 6 and 7 on April 4, 1993, were used for these calculations. During track # 6, the Learjet was flying within the cloud mass. The *in situ* observations collected during this time were used to validate the retrieved optical depth. During track # 7, the Learjet was flying near the cloud top. The *in situ* observations collected during this time were used to validate the retrieved mean effective ice crystal size. Cloud geometric depth was inferred from the Learjet pilot notes [*Williams*, 1993]. Radiation and microphysical measurements carried out during SUCCESS, specifically during track # 7 on April 21 1996, were also used for analysis. Cloud geometric thickness was obtained from the lidar onboard the NASA ER-2 aircraft. Note that for the SUCCESS case, we found only one instance of MAS and 2-DC measurements collocated in space and time. The discrepancies readily displayed in Fig. 1 could be a result of the physical assumptions and extrapolations used in the present retrieval methodology as well as approximations used in the validation study. Some of these issues are examined further in the following.

3. Uncertainty Estimates

Errors in the retrieved parameters, both random and biased, can be attributed to a number of factors, including limitations due to instrument performance and the physical assumptions inherent in the retrieval method. The results of a sensitivity study concerning the effects of the assumptions associated with the size and shape distributions of cirrus cloud particles and the complex nature of the surface reflectance (i.e., Lambertian surface assumption) are presented below. Subsequently, the vertical inhomogeneity of cirrus clouds is examined by using microphysical data collected *in situ*.

3.1. Sensitivity to Ice Crystal Size Distribution

In order to carry out theoretical computations and comparisons of the ice crystal scattering properties integrated over ensembles, it is useful to define some standard analytic size distributions. For the present study, four different types of common distributions were considered. Parameters for the various distributions were then calculated to obtain a mean effective ice crystal size (D_e) of 50 μm and effective variances (V_e) of 0.1 and 0.25, defined as:

$$V_e = \frac{1}{D_e^2} \frac{\int_{L_1}^{L_2} (\sqrt[3]{D^2 L} - D_e)^2 \, DLn(L)dL}{\int_{L_1}^{L_2} DLn(L)dL}, \tag{9}$$

where D is the width of an ice crystal determined from the *Auer and Veal* [1970] model. Note that for the purpose of these calculations, all ice crystals were assumed to be columnar in shape.

First, the following standard gamma size distribution is selected following *Hansen and Travis* [1974]:

$$n(L) = \frac{(ab)^{(2b-1)/b}}{\Gamma[(1-2b)/b]} L^{(1-3b)/b} \exp(-L/ab), \tag{10}$$

where a = D_e , b = V_e , and Γ is the gamma function. For this distribution, the parameters are given by a = 50 μm and b = 0.1 and 0.25.

Second, we use a bimodal distribution defined by

$$n(L) = \frac{L^{(1-3b)/b} \exp(-L/a_1 b)}{(a_1 b)^{(1-2b)/b} \Gamma[(1-2b)/b]} + \frac{L^{(1-3b)/b} \exp(-L/a_2 b)}{(a_2 b)^{(1-2b)/b} \Gamma[(1-2b)/b]}, \tag{11}$$

where each of the two parts has the same value of b and contains half of the ice crystal sizes. The parameters of the size distribution can then be obtained from

$$D_e = a_1 \left[\frac{1+(a_2/a_1)^3}{1+(a_2/a_1)^2} \right], \qquad V_e = \frac{\left[1+(a_2/a_1)^4\right]\left[1+(a_2/a_1)^2\right]}{\left[1+(a_2/a_1)^3\right]^2}(1+b)-1. \tag{12}$$

The relationship between the two peaks of the distribution was chosen arbitrarily as a_2/a_1 = 5. Thus, for D_e = 50 μm, a_1 = 10.3 μm and a_2 = 51.5 μm. For V_e = 0.1, b = 0.073, while for V_e = 0.25, b = 0.22.

Third, the log-normal distribution is employed:

$$n(L) = \frac{1}{\sqrt{2\pi}\sigma_g L} \exp\left(\frac{-(\ln L - \ln L_g)^2}{2\sigma_g^2} \right), \tag{13}$$

where

$$L_g = D_e(1+V_e)^{5/2}, \qquad \sigma_g = \ln(1+V_e). \tag{14}$$

Finally, the power law distribution is generated as an inverse cubic function as follows:

$$n(L) = 2\frac{L_1^2 L_2^2}{L_2^2 - L_1^2} L^{-3}, \tag{15}$$

for $L_1 < L < L_2$, and $n(L)$ = 0 otherwise. The parameters of the size distribution are given by

$$D_e = \frac{L_2 - L_1}{\ln\left(L_2 / L_1\right)}, \qquad V_e = \frac{L_2 + L_1}{2(L_2 - L_1)}. \tag{16}$$

Thus, for D_e = 50 μm and V_e = 0.1, L_1 = 27.5 μm and L_2 = 82.4 μm. Similarly, for D_e = 50 μm and V_e = 0.25, L_1 = 18.1 μm and L_2 = 106.9 μm. All of the size distributions were normalized so that

$$N = \int_0^\infty n(L)dL = 1.\text{m}^{-3}, \tag{17}$$

where N is the total number of ice crystals per unit volume. Normalization of the size distributions is necessary in order to avoid affecting the extinction coefficient and optical depth, which depend on the total number of ice crystals. The size distributions described in this section are illustrated in Fig. 2.

Single-scattering calculations were carried out for individual ice crystals (columns) ranging from 5 to 120 μm in size, at a 5 μm resolution for the 0.65, 1.6, and 2.2 μm wavelengths. The single scattering parameters were integrated over the number concentration distributions. Results indicate that the single-scattering albedo, the asymmetry parameter, and the phase function do not have significant sensitivity to the size distribution and its variance. Shown in Fig. 3, panels (a) and (b), are the phase functions for the four size distributions and effective variances described above. It is clear that the specific features such as differences in forward, backscattering, 22°, and 46° peaks are not substantial.

Using the scattering properties of the four distribution functions and two effective variances, theoretical calculations of the bidirectional reflectance were carried out for two different surfaces and three sun/satellite viewing geometries. The two backgrounds considered were Lambertian with isotropic reflectance of 6% (ocean) and 20% (land). The viewing geometries considered for the present calculations are given in Table 1. In order to assess the effect of the size distribution function and

effective variance on the retrieved optical depth, values of the combined visible (0.65 μm) surface/cloud bidirectional reflectance were calculated for 8 different cirrus optical depths, ranging from 0.1 to 16, for the four analytic size distributions and for mean effective variances of 0.1 and 0.25. Synthetic retrievals of the optical depth were conducted for three arbitrarily fixed values of reflectance (0.25, 0.5, and 0.75) using the reflectance tables obtained from theoretical calculations. The results of these retrievals are presented in Table 2. Intercomparison of these results as a function of the assumed variance, distribution type, and viewing geometry shows maximum differences in the retrieved optical depths of 0.05, 0.09, and 0.28 for fixed reflectances of 0.25, 0.5, and 0.75, respectively, corresponding to maximum relative retrieval errors of 1 to 3%. Based on the preceding studies, the size distribution appears to have little impact on the retrieved optical depth.

3.2 Sensitivity to Ice Crystal Habit

In order to determine the sensitivity of the retrieved parameters to various assumptions of ice crystal habit models, 12 representative size distributions (six for both tropical and midlatitude cirrus) with effective mean ice crystal size ranging from 21 to 123 μm were used. Scattering and absorption calculations were carried out for the three habit models listed in Table 3. Analysis of these calculations reveals that the assumed habit model can have significant effects on the single scattering parameters and phase functions. The near IR (1.6 μm) phase functions for the three habit models are plotted in Fig. 3(c) for a representative size distribution. Consistent differences are present in the scattering intensities for scattering angles in the satellite remote sensing range. For instance, scattering intensities for the pristine model are about twice the values for the aggregate model at the scattering angle of 50°. Inspection of the visible (0.65 μm) phase functions reveals differences in the scattering intensities primarily at scattering angles smaller than 30°. Thus, we would expect that the effects of the ice crystal habit model assumptions on the size parameter retrieval are significant.

In order to further quantify the single-scattering effects in terms of the retrieved quantities, computations of the combined cirrus-surface bidirectional reflectance were undertaken for the 12 mean effective ice crystal sizes, three habit models, and cirrus optical depths ranging from 0.1 to 16. These calculations were carried out for two different sun/sensor geometry combinations corresponding to two

field experiment cases: track #7 on April 21, 1996 (θ_0 = 26°, $\Delta\phi$ = 46.5°), during SUCCESS, and track #7 on April 4, 1993 (θ_0 = 21°, $\Delta\phi$ = 51.5°), during CEPEX. Note that the background surface for SUCCESS is land, while the background surface for CEPEX is ocean. Cloud base reflectances were obtained from analysis of the clear pixel histograms of reflectance generated from the 100 scanlines surrounding the data points considered. Values of the combined bidirectional reflectance from theoretical calculations are presented in Fig. 4 for the three ice crystal habit models. Overlying these theoretical calculations are data points of the reflectances corresponding to cirrus observed on the days considered. Retrievals were carried out for these sample data points with the results presented in Table 4.

Synthetic retrievals were conducted for optical depths ranging from 0.1 to 8, and mean effective ice crystal sizes ranging from 20 to 100 μm, using the sun/sensor viewing geometry combinations listed in Table 1. In Fig. 5, differences in the retrieved values averaged over the five sun/sensor geometries are presented. The habit model assumptions can result in relative errors on the order of 5% for the retrieved optical depth, and in absolute errors of 10 to 20 μm for the retrieved mean effective ice crystal size. Thus, the ice crystal shape assumptions can introduce a moderate error in the retrieved optical depth and a significant error in the retrieved mean effective ice crystal size.

The preceding calculations were carried out assuming that ice crystals have smooth surfaces. In order to assess the impact of ice crystal surface roughness on the retrieved cloud parameters, scattering/absorption and radiative transfer calculations were performed for the 12 mean effective sizes used in the previous section, based on mixed and pristine habit models for the same two field experiment cases. Calculations showed that surface roughness can have a significant impact on the phase function for ice crystals. Near IR (1.6 μm) phase functions for the pristine habit model using a representative size distribution are displayed in Fig. 3(d) for both smooth and rough ice crystal surface assumptions. The backscattering, 22°, and 46° peaks vanish for rough surface ice crystals. Furthermore, a significant decrease in the scattering intensity can be seen throughout most of the scattering angle range that is useful for satellite remote sensing applications. Similar trends are also observed for the visible (0.65 μm) incident radiation. Thus, we would expect that surface roughness assumptions could have a significant effect on both the retrieved optical depth and mean effective ice crystal size.

Values of the combined bidirectional reflectance based on theoretical calculations are presented in Fig. 6. Overlying these theoretical calculations are data points of reflectance corresponding to the observed cirrus for the field experiment days considered. The retrieval results are presented in Table 5. Synthetic retrievals were carried out using optical depths from 0.1 to 8 and mean effective ice crystal sizes from 20 to 100 μm and involving the sun/sensor viewing geometry combinations listed in Table 1. Comparisons of the results for ice crystals assumed to have smooth surfaces with those assumed to have rough surfaces are shown in Fig. 7. Consistent differences in the retrieved size and optical depth of 5 to 10 μm and 5 to 10%, respectively, are displayed. It is clear that the assumptions of ice crystal surface roughness can potentially introduce substantial errors in both the retrieved optical depth and mean effective ice crystal size.

3.3. Sensitivity to surface reflectance

To calculate the combined bidirectional reflectance from the surface/atmosphere/cloud system, values of the surface reflectance with atmospheric correction must be known. To infer these values, clear pixel reflectances are analyzed, and a single value is typically selected for each channel used in the retrieval [e.g., *Wielicki et al*., 1990; *Nakajima et al*., 1991; *Rolland and Liou*, 1998]. This approach is illustrated in Fig. 8(a) in which the data were collected on April 16, 1996, track # 7 (land background surface) during SUCCESS. Clear pixel reflectance values for the three channels used in the present method have been organized in the form of histograms. When a single distinct peak exists (e.g., 0.6 μm channel), the corresponding reflectance value is selected. When a number of frequency peaks coexist (e.g., 1.6 and 2.2 μm channels), a weighted average of the corresponding data provides the necessary reflectance values. The major drawback associated with this method is that the natural anisotropy and variance of the background surface are not accounted for. To illustrate this point, the reflectances collected over 100 scan lines in the clear portion of track # 7 were averaged pixel by pixel, and displayed as a function of sensor scan angle (-43° to +43° for the MAS) as shown in Fig. 8b. Also displayed for reference are the values obtained from the histogram analysis. Significant variance in the data set is evident. In order to characterize the error introduced, we compute the standard deviation σ of the reflectance data set from each of the spectral values corresponding to the three channels obtained from the histogram analysis. A

similar analysis was carried out for an ocean surface background scene observed on May 12, 1996, track # 13, during SUCCESS. Results for this case are presented in Fig. 9. The reflectance and standard deviation values obtained from the analysis of these two cases are listed in Table 6.

To quantify the impact of the natural background surface reflectance on cirrus cloud property retrievals, two sets of combined surface/cirrus bidirectional reflectance lookup tables were computed for each of the two SUCCESS cases considered. The appropriate standard deviation was added to the surface reflectance for one set, and subtracted for the other. These calculations are illustrated for one viewing geometry (nadir) in Fig. 10. Panels (a) and (b) correspond to the land surface case, while panels (c) and (d) are associated with the ocean surface case. The overlying data points are for the cirrus clouds observed during the course of these tracks. Retrievals of the optical depth and mean effective ice crystal size were carried out using the two lookup tables for each of the observed data points. Results are given in Tables 7 and 8. It is clear that the complex nature of land surfaces must be accounted for to avoid producing large errors in the retrieved parameters, particularly for thin cirrus with $\tau < 2$ for which the theoretical calculations significantly differ. The bidirectional reflectance sensitivity to the variance of the background reflectance is actually greater than the overall sensitivity of the cloud reflectance to the parameters used for retrieval. Errors introduced in the case of the ocean background are much smaller. However, it is noted that in order to reliably retrieve the mean effective ice crystal size of thin cirrus over oceans, the anisotropy of ocean surfaces must be accounted for.

3.4 Sensitivity to vertical inhomogeneity of tropical anvils

Midlatitude stratified cirrus clouds are frequently associated with large-scale ascending motions. Tropical cirrus anvils, on the other hand, are commonly generated by deep convective cells. Thus, the extremely long wet trajectories characteristic of tropical cumulonimbi involve complex microphysics embedded in strong mesoscale convection. In extreme cases, the cloud base can be 100°C warmer and 10,000 times wetter than the cloud top [*Knollenberg* et al., 1993]. Since the significant vertical inhomogeneity is apparent for tropical cirrus, it is important to examine the effect this may have on the microphysical characteristics of these clouds.

The 2-DC data for three representative anvil cases (developing, mature, and dissipating) collected *in*

situ during CEPEX were acquired to characterize the vertical structure of the observed ice crystal populations [*McFarquhar and Heymsfield,* 1996]. 2270 size distributions were classified in eight temperature bins, ranging from -20 to -60°C, for each of the three cases considered. An average size distribution and the associated standard deviation were computed for each of the temperature bins. The results of these calculations are displayed in Fig. 11. Using this statistical analysis, a number of microphysical properties were calculated for each of the 24 representative size distributions. Displayed in Table 9 are the mean effective ice crystal sizes, ice water contents, and extinction coefficients and their standard deviations. The extinction coefficient was calculated from the parameterization equation developed by *Fu and Liou* [1993]:

$$\beta_e = IWC \sum_{n=0}^{2} \frac{a_n}{D_e^n}, \tag{18}$$

where a_0 = -6.656x10^{-3}, a_1 = 3.686, and a_2 = 0 for the wavelengths pertinent to the present study. The extinction coefficient varies by about one order of magnitude between the lowest and highest temperature bins. This would have important implications in remote sensing validation studies. Typically, *in situ* measurements are available from one or a limited number of in-cloud flight levels. These measurements must then be extrapolated over the whole cloud depth. Significant discrepancies can thus be introduced between the cloud optical depth calculated from observed data and that of the actual cloud. In order to illustrate this point, the optical depths of the three anvil cases and their standard deviations were calculated as follows:

$$\tau = \sum_{j=1}^{8} \beta_{e,j} \Delta z_j, \tag{19}$$

where $\beta_{e,j}$ and Δz_j are the extinction coefficient and cloud thickness, respectively, for the j height interval. The height interval values corresponding to the eight temperature bins for the three cases were obtained from the Rosemount temperature sensor and Learjet altitude data. For the three anvil cases, eight optical depths and the associated standard deviations were also calculated for the eight temperature bins by extrapolating each of the eight extinction coefficients throughout the depth of the cloud. This approach would be employed in validation studies when only one extinction coefficient value is available. The results of these calculations are displayed in Fig. 12. In all three cases, the optical depth varies

significantly in the vertical and it can be seen that the greatest error would be introduced for the mature case. This illustrates the need to use multiple in-cloud flight level data in the validation studies for thick cirrus clouds.

4. CONCLUSIONS

A solar reflectance retrieval method has been developed for the remote sensing of cirrus cloud properties using MAS channels. Validation efforts were carried out, emphasizing the need to further understand and quantify the nature of the errors inherent in the assumptions employed in the method. First, the errors introduced by various assumptions in the microphysical models were investigated. The variance and aspect of the size distribution were found to have little impact on the retrieved optical depth. Thus, retrieving the effective variance of the size distribution from solar reflectance measurements at 0.65, 1.6, and 2.2 μm may not be practically possible.

The effect of the ice crystal shape on the retrieved mean effective ice crystal size is important and must be properly accounted for when developing lookup tables of bidirectional reflectances. The potential impact of ice crystal surface roughness on the retrieval results was also demonstrated. In the last two decades, microphysical observations collected over the course of field experiments carried out around the globe have helped to better characterize the nature of the size distributions of ice crystals, both in the midlatitudes [e.g., *Heymsfield and Platt*, 1984] and in the tropics [e.g., *McFarquhar and Heymsfield*, 1997]. The present study suggests that characterizing the nature of ice crystals in terms of their intrinsic properties involving shape and surface roughness is equally significant for applications to remote sensing.

In order to accomplish reliable retrievals of the microphysical and optical properties of thin cirrus using solar reflectance techniques, the background surface reflectance must be accounted for in a precise manner, especially over complex land surfaces. Finally, analysis of the microphysical and radiative properties of three cirrus anvils were used to illustrate the vertical inhomogeneity of thick cirrus which must be accounted for in validation efforts.

Acknowledgments. This research was supported by NASA grants ESS/97-0062, NAG5-6160, NAG5-7738, and NAG1-1966. We thank Dr. P. Yang for providing the single-scattering model and Dr. Y. Takano for providing the radiative transfer model used in this study.

References

Ackerman, S. A., W. L. Smith, J. D. Spinhirne, and H. E. Rivercomb, The 27-28 October 1986 FIRE IFO cirrus case study: spectral properties of cirrus clouds in the 8-12 μm window, *Mon. Wea. Rev.,* 118**,** 2377-2388, 1990.

Auer, H. A., and D. L. Veal, The dimension of ice crystal in natural clouds, *J. Atmos. Sci.,* 45, 919-926, 1970.

Blau, H. H., R. P. Espinola, and E. C. Reifenstein, Near infrared scattering by sunlit terrestrial clouds. *Appl. Opt.,* 5, 555-564, 1966.

Cline, A. K., Scalar-and-planar-valued curve fitting using splines under tension. *Assoc. Comput. Mach. Commun.,* 17, 218-220, 1974.

Fu, Q, and K. N. Liou, Parameterization of the radiative properties of cirrus clouds. *J. Atmos. Sci.,* 50, 2008-2025, 1993.

Hansen, J. E., and J. B. Pollack, Near infrared light scattering by terrestrial clouds. *J. Atmos. Sci.,* 27, 265-281, 1970.

Hansen, J. E, and L. D. Travis, Light scattering in planetary atmospheres, *Space Sci. Rev.,* 16, 527-610, 1974.

Heymsfield, A.J., and R.G. Knollenberg, Properties of cirrus generating cells. *J. Atmos. Sci.,* 29, 1358-1366, 1972.

Heymsfield, A. J., and C. M. R. Platt, A parameterization of the particle size spectrum of ice clouds in terms of ambient temperature and ice water content, *J. Atmos. Sci.,* 41, 846-855, 1984.

Iaquinta,J., and P. Personne, Theoretical scattering function of bullet rosette ice cystals. *Fifth ICE/EUCREX Workshop,* Clermont-Ferrand, France, p. 143, 1992.

Inoue, T., 1985: On the temperature and effective emissivity determination of semi-transparent cirrus clouds by bispectral measurements in the 10 μm window region. *Meteorol. Soc. Japan,* 63, 88-99, 1985.

King, M. D., S.C. Tsay, S. E. Platnick, M. Wang, and K.N. Liou, Cloud retrieval algorithms for MODIS: Optical thickness, effective particle radius, and thermodynamic phase. *MODIS Algorithm Theoretical Basis Document No. ATBD-MOD-05 MOD-06 – Cloud Product.* Version 5, 1997 [available from ftp://eospso.gsfc.nasa.gov/ATBD/REVIEW/MODIS/ATBD-MOD-05/atbd-mod-05.pdf]

King, M. D., W. P. Menzel, P. S. Grant, J. S. Myers, G. T. Arnold, S. E. Platnick, L. E. Gumley, S.C. Tsay, C. C. Moeller, M. Fitzgerald, K. S. Brown and F. G. Osterwisch, Airborne scanning spectrometer for remote sensing of cloud, aerosol, water vapor and surface properties. *J. Atmos. Oceanic Technol.,* 13, 777-794, 1996.

Knollenberg, R. G., K. Kelly, and J. C. Wilson, Measurements of high number densities of ice crystals in the tops of tropical cumulonimbus. *J. Geophys. Res.,* 98, 8639-8664, 1993.

Liou, K. N., On the radiative properties of cirrus in the window region and their influence on remote sensing of the atmosphere. *J. Atmos. Sci.,* 31, 522-532, 1974.

Liou, K. N., An introduction to atmospheric radiation. *Academic Press,* 392 pp, 1980.

Liou, K. N., Influence of cirrus clouds on weather and climate processes: A global perspective, *Mon. Wea. Rev.,* 114, 1167-1199, 1986.

Liou, K. N., Radiation and cloud processes in the atmosphere. *Oxford University Press,* 487 pp, 1992.

Liou, K. N., S. C. Ou, Y. Takano, F. P. J. Valero, and T. P. Ackerman, Remote sounding of the tropical cirrus cloud temperature and optical depth using 6.5 and 10.6 μm radiometers during STEP. *J. Appl. Meteor.,* 29, 716-726, 1990.

Liou, K. N., and Y Takano, Light scattering by nonspherical particles: Remote sensing and climatic implications. *Atmos. Res.,* 31, 271-298, 1994.

McFarquhar, G. M., and A. J. Heymsfield, Microphysical characteristics of three cirrus anvils sampled during the central equatorial pacific experiment (CEPEX), *J. Atmos. Sci.*, 52, 4143-4158, 1996.

McFarquhar, G. M., and A. J. Heymsfield, Parameterization of tropical cirrus ice crystal size distributions and implications for radiative transfer: Results from CEPEX, *J. Atmos. Sci.,* 54, 2187-2200. 1997.

McFarquhar, G. M., A. J. Heymsfield, A. Macke, J. Iaquinta, and S. M. Aulenbach, Use of observed ice crystal sizes and shapes to calculate mean scattering properties and multi-spectral radiances: CEPEX 4 April 1993 case study, *J. Geophys. Reas.,* Submitted, 1999.

Mitchell, D.L., R. Zhang, and R.L. Pitter, Mass-dimensional relationships for ice particles and the influence of riming on snowfall rates. *J. Appl. Meteor.,* 29, 153-163, 1990.

Nakajima, T., and M. D. King, Determination of the optical thickness and effective particle radius of clouds from reflected solar radiation measurements. I—Theory. *J. Atmos. Sci.,* 47, 1878-1893, 1990.

Nakajima, T., M. D. King, J. D. Spinhirne, and L. F. Radke, Determination of the optical thickness and effective particle radius of clouds from reflected solar radiation measurements. II—Marine stratocumulus observations, *J. Atmos. Sci.,* 48, 728-750, 1991.

Ou, S. C., K. N. Liou, W. M. Gooch, and Y. Takano, Remote sensing of cirrus cloud properties using AVHRR 3.7 and 10.9 μm channels. *Appl. Opt.*, 32, 2171-2180, 1993.

Ou, S. C., and Coauthors, Remote sounding of cirrus cloud optical depths and ice crystal sizes from AVHRR data: Verification using FIRE-II-IFO measurements. *J. Atmos. Sci.,* 52, 4143-4158, 1995.

Personne, P., Ch. Duroure, C. Isaka, and H. Isaka, Geometrical characteristics of bullet-rosette ice cystals. IAMAP *Program and Abstracts*, p. 39, 1991.

Rao, N. X., S. C. Ou, and K. N. Liou, Removal of the solar component in AVHRR 3.7 μm radiances for the retrieval of cirrus cloud parameters. *J. Appl. Meteor.,* 34, 482-499, 1995.

Rolland, P., and K. N. Liou, Remote sensing of optical and microphysical properties of cirrus clouds using MODIS channels, in *Cirrus,* OSA Technical Digest, pp. 17-19, Optical Society of America, Washington DC, 1998.

Takano, Y., and K. N. Liou, Radiative transfer in cirrus clouds. I. Single-scattering and optical properties of hexagonal ice crystals, *J. Atmos. Sci.,* 46, 3-19, 1989a.

Takano, Y., and K. N. Liou, Radiative transfer in cirrus clouds. II. Theory and computation of multiple scattering in an anisotropic medium, *J. Atmos. Sci.,* 46, 20-36, 1989b.

Takano, Y., and K. N. Liou, Radiative transfer in cirrus clouds. III. Light scattering by irregular ice crystals. *J. Atmos. Sci.,* 52, 818-837, 1995.

Twomey, S., and K. J. Seton, Inferences of gross microphysical properties of clouds form spectral reflectance measurements. *J. Atmos. Sci.,* 37, 1065-1069, 1980.

Twomey, S., and T. Cocks, Spectral reflectance of clouds in the near-infrared—Comparison of measurements and calculations. *J. Meteorol. Soc. Japan,* 60, 583-592, 1982.

Twomey, S., and T. Cocks, Remote sensing of cloud parameters from spectral reflectance in the near-infrared. *Beitr. Phys. Atmos.,* 62, 172-179, 1989.

Wielicki, B. A., J. T. Suttles, A. J. Heymsfield, R. M. Welch, J. D. Spinhirne, M. L. C. Wu, and D. O. Starr, The 27-28 October 1986 FIRE IFO cirrus case study: Comparison of radiative transfer theory with observations by satellite and aircraft, *Mon. Wea. Rev.,* 118, 2356-2376, 1990.

Wielicki, B. A., R. D. Cess, M. D. King, D. A. Randall, and E. F. Harrison, Mission to Planet Earth: Role of clouds and radiation in climate, *Bull. Amer. Meteor. Soc.,* 76, 2125-2153, 1995.

Williams, S. F., Central Equatorial Pacific Experiment (CEPEX) daily operations summary, 321, University Corporation for Atmospheric Research, Boulder, Co., 1993.

Yang, P., and K.N. Liou, A geometric-optics/integral equation method for light scattering by nonspherical ice crystals, *Appl. Opt.*, 35, 6568-6584, 1996.

Yang, P., K.N. Liou, and W.P. Arnott, Extinction efficiency and single-scattering albedo for laboratory and natural cirrus clouds, *J. Geophys. Reas.,* 102, 21825-21835, 1997.

K. N. Liou and P. Rolland, Department of Atmospheric Sciences, 7127 Math Science Building, 405 Hilgard Avenue, University of California, Los Angeles, CA 90095-1565, (email: prolland@atmos.ucla.edu)

M. D. King and S. C. Tsay, NASA Goddard Space Flight Center, Code 900, Greenbelt, MD 20771.

G. M. McFarquhar, National Center for Atmospheric Research, P.O. Box 3000, Boulder, CO 80307-3000.

Figure Captions

Figure 1. Comparison of the retrieved parameters with those derived from analysis of *in situ* data collected during CEPEX (April 4 1993, tracks # 6 and 7) and SUCCESS (April 21 1996, track # 7). Also shown for illustration of the collocation process are two examples from CEPEX and SUCCESS of visible (0.65 μm) imagery overlaid with aircraft paths and 2-DC data measurement locations.

Figure 2. Gamma (a), bimodal (b), log-normal (c), and power (d) size distributions having identical mean effective ice crystal size (50 μm) and two different values of effective variance (0.1 and 0.25). The ice crystal size distributions are normalized.

Figure 3. Visible (0.65 μm) phase functions for the four analytic size distributions (a) and three effective size distribution variances (b). Near IR (1.6 μm) phase functions for three ice crystal habit models (c) and two ice crystal surface conditions (d). Note that for presentation purposes the phase function values for angles less than 1° are not plotted.

Figure 4. Correlation of the theoretical bidirectional reflectance for 0.65 and 1.6 μm (panels a and c) and for 0.65 and 2.2 μm (panels b and d) using cloud optical depths ranging from 0.1 to 8. Panels a and b and panels c and d are for tropical and midlatitude size distributions, respectively. The three sets of curves correspond to calculations for the three different habit assumptions. Superimposed data points are from MAS measurements.

Figure 5. Average absolute errors in the retrieved optical depth (a) and mean effective ice crystal size (b) produced by assumed ice crystal shape.

Figure 6. Correlation of the theoretical bidirectional reflectance for 0.65 and 1.6 μm using mixed (panels a and c) and pristine (panels b and d) ice crystal habit models for cloud optical depths ranging from 0.1 to 8. Panels a and b and panels c and d are for tropical and midlatitude size distributions, respectively. The two sets of curves correspond to calculations carried out for the two different ice crystal surface roughness assumptions. Superimposed data points are from MAS measurements.

Figure 7. Average absolute errors in the retrieved optical depth (a) and mean effective ice crystal size (b) produced by ice crystal surface roughness.

Figure 8. (a) Clear pixel reflectance histograms for the land surface case. Results are presented for the three channels used in the retrieval. (b) Clear pixel reflectances for 100 scan lines for the land surface case, averaged and displayed as a function of sensor scan angle. Results are presented for the three channels used in the retrieval.

Figure 9. Same as Fig. 7, except for the ocean surface case.

Figure 10. Correlation of the bidirectional reflectance for 0.65 and 1.6 μm (panels a and c) and for 0.65 and 2.2 μm (panels b and d) for the six midlatitude size distributions. Calculations are presented for the surface reflectance values obtained from analysis of the clear pixel histograms, plus or minus one standard deviation. Panels (a) and (b) correspond to the land surface case (track # 7, April 16 1996). Panels (c) and (d) correspond to the ocean surface case (track # 13, May 12 1996).

Figure 11. Averaged size distributions from the three anvil cases as a function of ambient temperature. The error bars represent the calculated number concentration standard deviations.

Figure 12. Optical depths and the associated standard deviations calculated from integration in the vertical of the eight temperature levels extinction coefficients (straight line) and from each of the eight extinction coefficient values extrapolated over the whole cloud depth (see text for details).

Table 1. Sun-Sensor Viewing Geometry Values Used in This Study

	1	*2*	*3*
θ_0 (°)	0	30	60
θ (°)	0	0	0
$\Delta\phi$ (°)	0	0	0

Table 2. Values of Optical Depth Retrieved from Bidirectional Reflectance Tables Calculated Using the Four Different Size Distribution Functions and Two Effective Variances. TheThree Sun-Satellite Geometries are Given in Table 1.

			Reflectance = 0.25			Reflectance = 0.5			Reflectance = 0.75		
			Geometry			Geometry			Geometry		
		V	1	2	3	1	2	3	1	2	3
Bimodal	Land	0.1	0.49	0.62	0.43	3.59	3.95	3.28	9.92	11.81	13.12
		0.25	0.5	0.61	0.43	3.62	3.92	3.26	10	11.71	13.04
	Ocean	0.1	1.76	1.94	1.32	4.88	5.19	4.36	12.6	14.28	15.4
		0.25	1.78	1.93	1.31	4.91	5.14	4.33	12.71	14.19	15.33
Gamma	Land	0.1	0.49	0.62	0.43	3.59	3.96	3.29	9.92	11.87	13.17
		0.25	0.5	0.61	0.43	3.6	3.92	3.26	9.96	11.71	13.04
	Ocean	0.1	1.76	1.95	1.33	4.9	5.21	4.38	12.63	14.33	15.44
		0.25	1.77	1.92	1.31	4.9	5.14	4.33	12.66	14.19	15.33
Log-normal	Land	0.1	0.47	0.62	0.43	3.52	3.96	3.29	9.71	11.87	13.17
		0.25	0.49	0.62	0.43	3.58	3.97	3.3	9.9	11.89	13.19
	Ocean	0.1	1.73	1.95	1.33	4.83	5.21	4.38	12.44	14.34	15.44
		0.25	1.76	1.95	1.33	4.89	5.22	4.38	12.62	14.36	15.46
Power	Land	0.1	0.5	0.61	0.43	3.61	3.92	3.26	9.99	11.71	13.05
		0.25	0.5	0.61	0.43	3.61	3.91	3.25	9.99	11.67	13.01
	Ocean	0.1	1.78	1.92	1.31	4.91	5.15	4.34	12.69	14.2	15.34
		0.25	1.78	1.92	1.31	4.9	5.13	4.32	12.69	14.15	15.3

Table 3. Ice Crystal Habit Models Used in This Study

	Pristine	*Aggregate*	*Mixed*
L < 100 μm	Plates	Bullet Rosettes	80% Plates 20% Columns
L > 100 μm	Columns	Column Aggregates	50% Columns 50% Rosettes

Table 4. Retrieval Results for the Three Ice Crystal Habit Models for the Two Observed Sample Data Points

		SUCCESS			CEPEX		
		Pristine	Aggregate	Mixed	Pristine	Aggregate	Mixed
Point # 1	D_e (μm)	94.9	109.1	101.6	37.0	37.2	37.0
	τ	1.94	1.89	1.91	1.39	1.36	1.37
Point # 2	D_e (μm)	98.1	111.9	105.0	82.9	100.1	92.9
	τ	6.13	6.09	6.08	7.87	7.75	7.79

Table 5. Retrieval Results for the Two Ice Crystal Surface Roughness Regimes, for the Two Observed Sample Data Points

		SUCCESS		CEPEX	
		Smooth	Rough	Smooth	Rough
Point # 1	D_e (μm)	101.6	103.6	82.2	85.3
	τ	1.91	1.80	1.37	1.29
Point # 2	D_e (μm)	105.0	109.2	94.9	98.9
	τ	6.08	5.75	7.79	7.36

Table 6. Reflectance Values from Histogram Analysis and Observed Standard Deviations for the Two SUCCESS Cases

	April 16, 1999		May 12, 1999	
	r_{cl}	σ	r_{cl}	σ
0.65 μm	0.16	0.03	0.04	0.005
1.6 μm	0.39	0.06	0.01	0.003
2.2 μm	0.28	0.04	0.01	0.004

Table 7. Retrieval Results for the Land Background Case.

	τ (-σ)	τ (+σ)	D_e (-σ)	D_e (+σ)
Point # 1	4	3.25	38	61
Point # 2	6.75	6.25	64	78

-σ and +σ correspond to one standard deviation subtracted and added to the clear pixel reflectance, respectively

Table 8. Retrieval Results for the Ocean Background Case

	τ (-σ)	τ (+σ)	D_e (-σ)	D_e (+σ)
Point # 1	.75	.75	39	65
Point # 2	2.75	2.5	62	60
Point # 3	4.5	4.5	70	72

-σ and +σ corresponds to one standard deviation subtracted and added to the clear pixel reflectance, respectively

Table 9. Mean Effective Crystal Size, Ice Water Content, Extinction Coefficient, and Associated Standard Deviations for the Eight Temperature Bins, for the Three Anvil Cases

T (^{o}C)	Developing Anvil				Mature Anvil				Dissipating Anvil			
	# SD	D_e (m)	IWC (10^{-2}g.m^{-3})	e (km^{-1})	# SD	D_e (m)	IWC (10^{-2}g.m^{-3})	e (km^{-1})	# SD	D_e (m)	IWC (10^{-2}g.m^{-3})	e (km^{-1})
-55 to -60	108	31.1 .4	0.41 .02	0.46 .05	102	26.3 .3	0.41 .02	0.55 .02	14	14.6 .01	0.34 .01	0.84 .02
-50 to -55	160	33.3 .4	1.15 .04	1.19 .03	76	29.8 .3	0.49 .16	0.57 .18	81	30.1 .4	0.63 .02	0.73 .01
-45 to -50	160	39.6 .8	1.45 .09	1.25 .05	28	83.2 .6	9.78 .50	3.68 .15	176	37.4 .9	0.73 .05	0.67 .03
-40 to -45	49	52.2 1.1	2.40 .16	1.53 .07	102	79.6 1.9	13.3 1.5	5.27 .45	189	52.0 1.7	1.02 .11	0.65 .05
-35 to -40	41	32.4 .3	0.37 .02	0.39 .02	25	67.7 .9	6.85 .31	3.27 .08	36	60.5 1.5	1.83 .13	0.99 .03
-30 to -35	116	62.9 1.2	5.26 .34	2.73 .11	31	75.8 .6	3.72 .20	1.56 .07	339	65.4 1.1	2.80 .21	1.39 .17
-25 to -30	9	72.7 3.0	6.17 .50	2.72 .08	75	76.8 .9	3.52 .19	1.46 .05	112	72.4 .9	1.10 .10	0.49 .04
-20 to -25	21	80.5 3.0	7.67 .70	3.00 .14	8	71.9 1.0	9.80 .42	4.37 .12	115	78.5 1.2	1.88 .16	0.76 .05

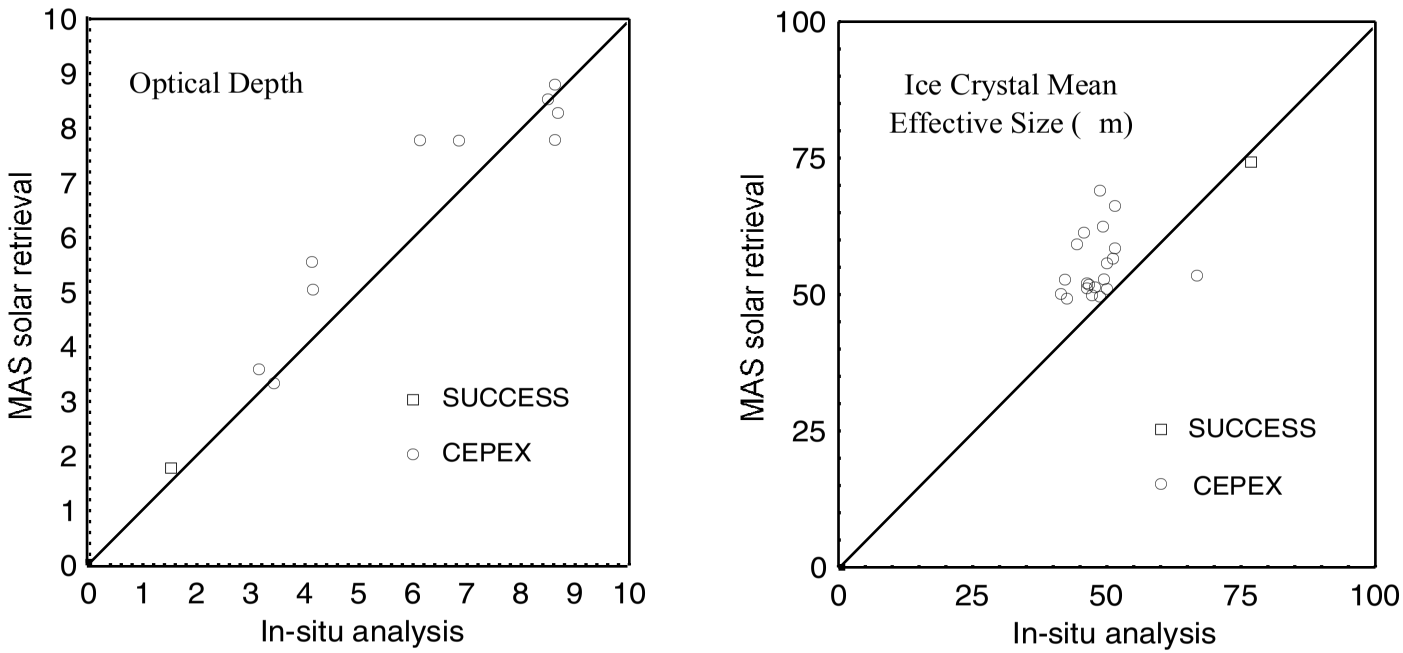
Optical Depth
MAS solar retrieval
In-situ analysis
SUCCESS
CEPEX
0
1
2
3
4
5
6
7
8
9
10
Ice Crystal Mean
Effective Size (m)
MAS solar retrieval
In-situ analysis
SUCCESS
CEPEX
0
25
50
75
100

Fig. 1a

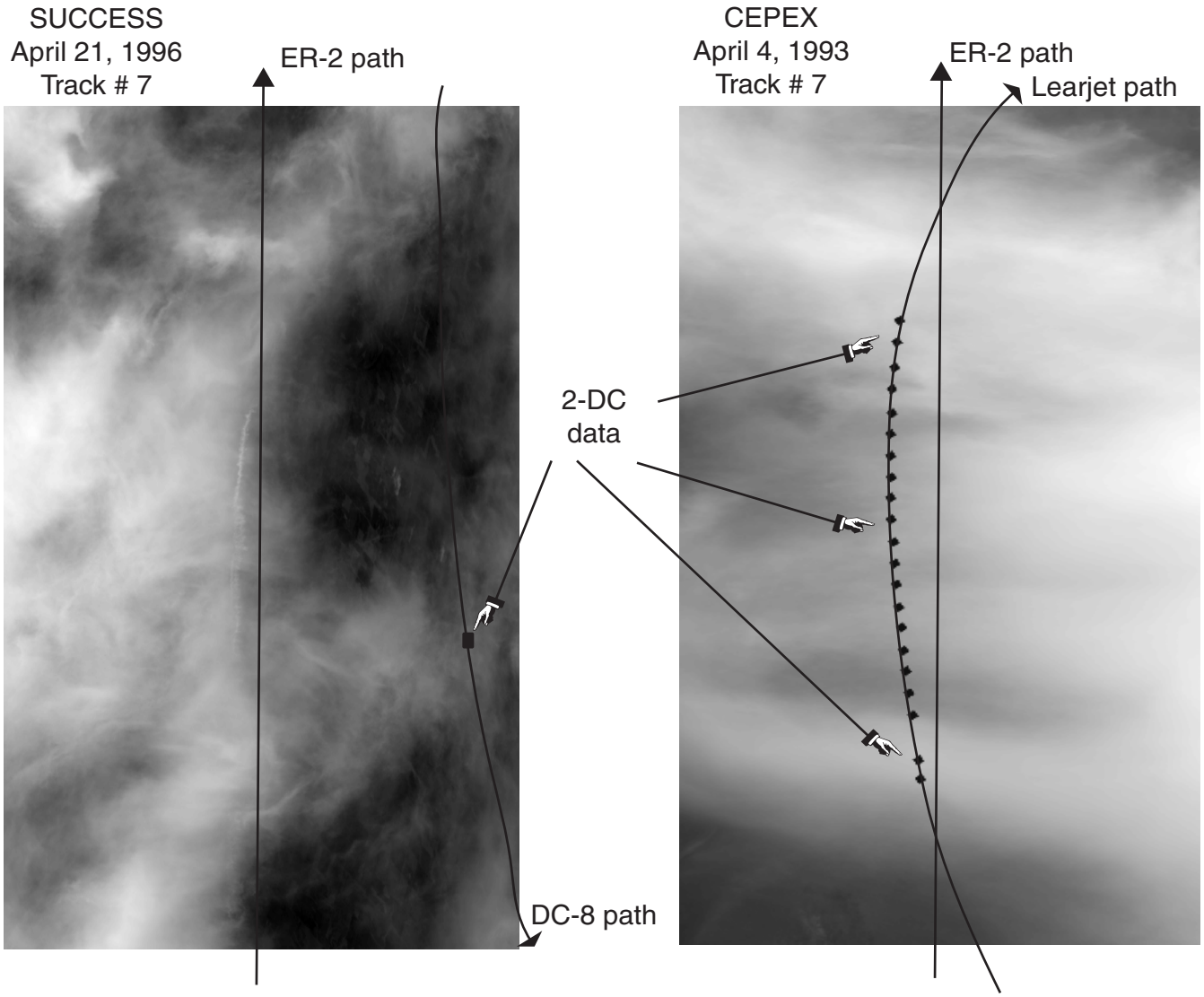
SUCCESS
April 21, 1996
Track # 7
ER-2 path
CEPEX
April 4, 1993
Track # 7
ER-2 path
Learjet path
2-DC
data
DC-8 path

Fig. 1b

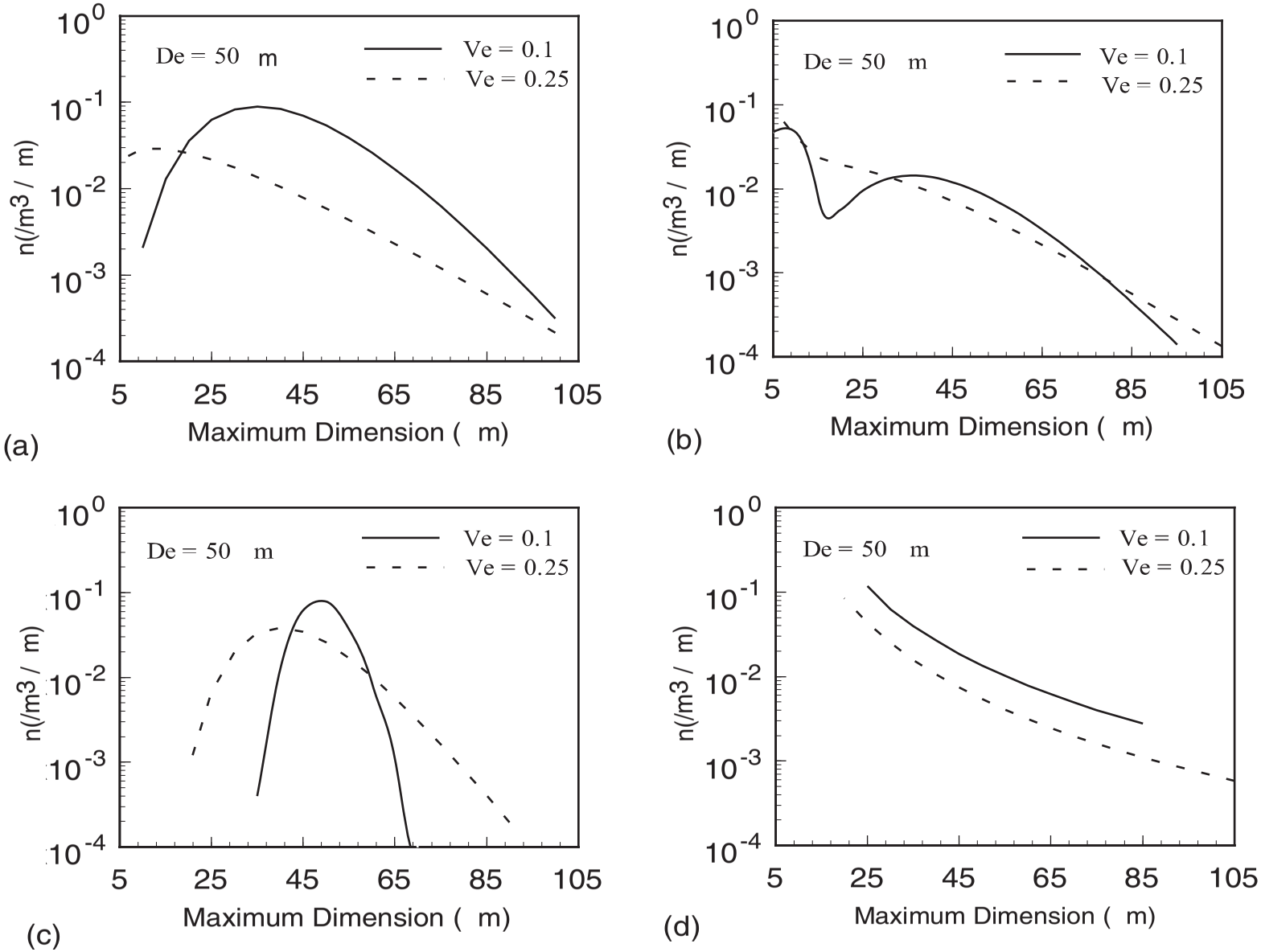

Fig. 2

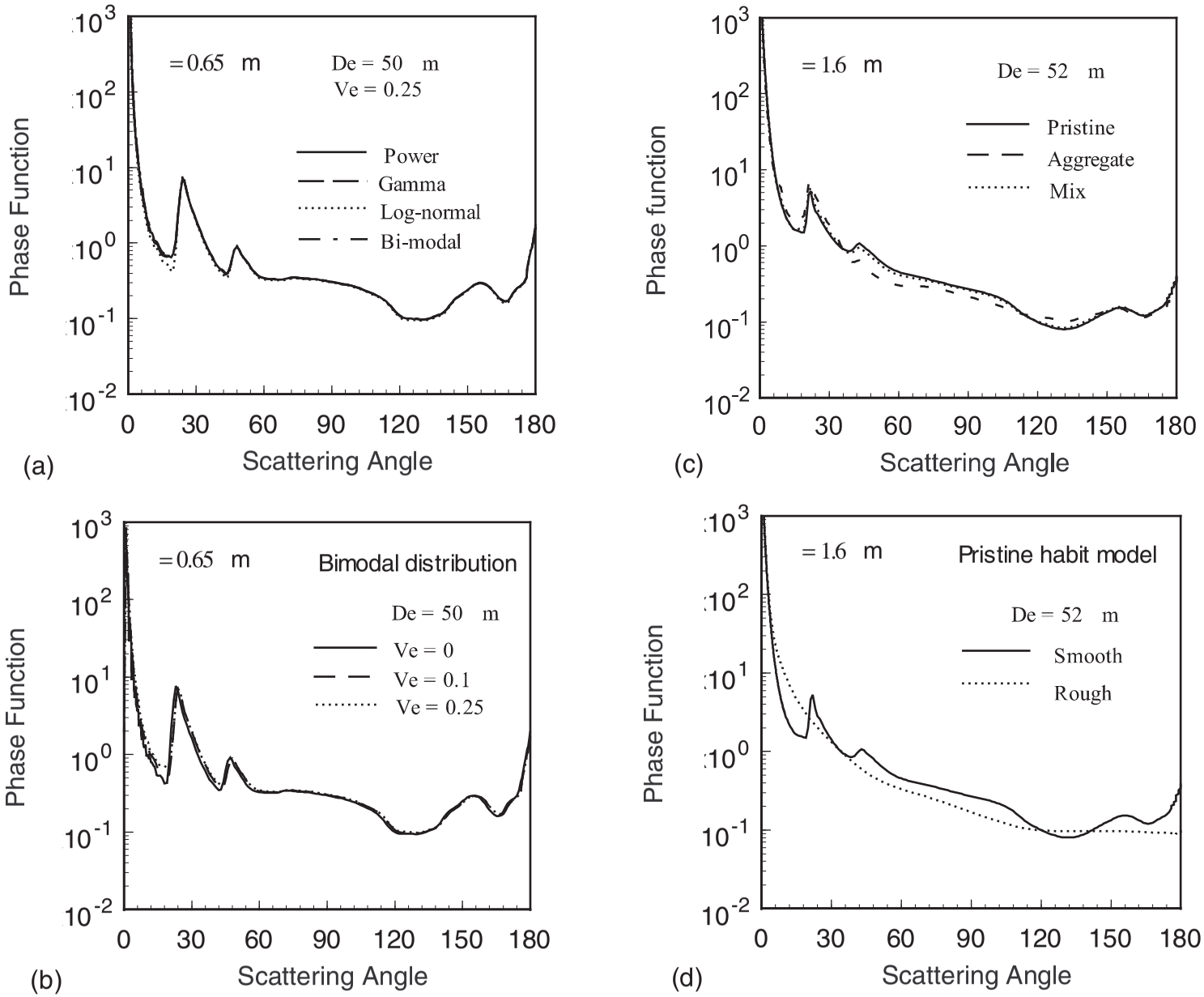
=0.65 m
De = 50 m
Ve = 0.25
Power
Gamma
Log-normal
Bi-modal
Phase Function
Scattering Angle
(a)
=1.6 m
De = 52 m
Pristine
Aggregate
Mix
Phase function
Scattering Angle
(c)
=0.65 m
Bimodal distribution
De = 50 m
Ve = 0
Ve = 0.1
Ve = 0.25
Phase Function
Scattering Angle
(b)
=1.6 m
Pristine habit model
De = 52 m
Smooth
Rough
Phase Function
Scattering Angle
(d)

Fig. 3

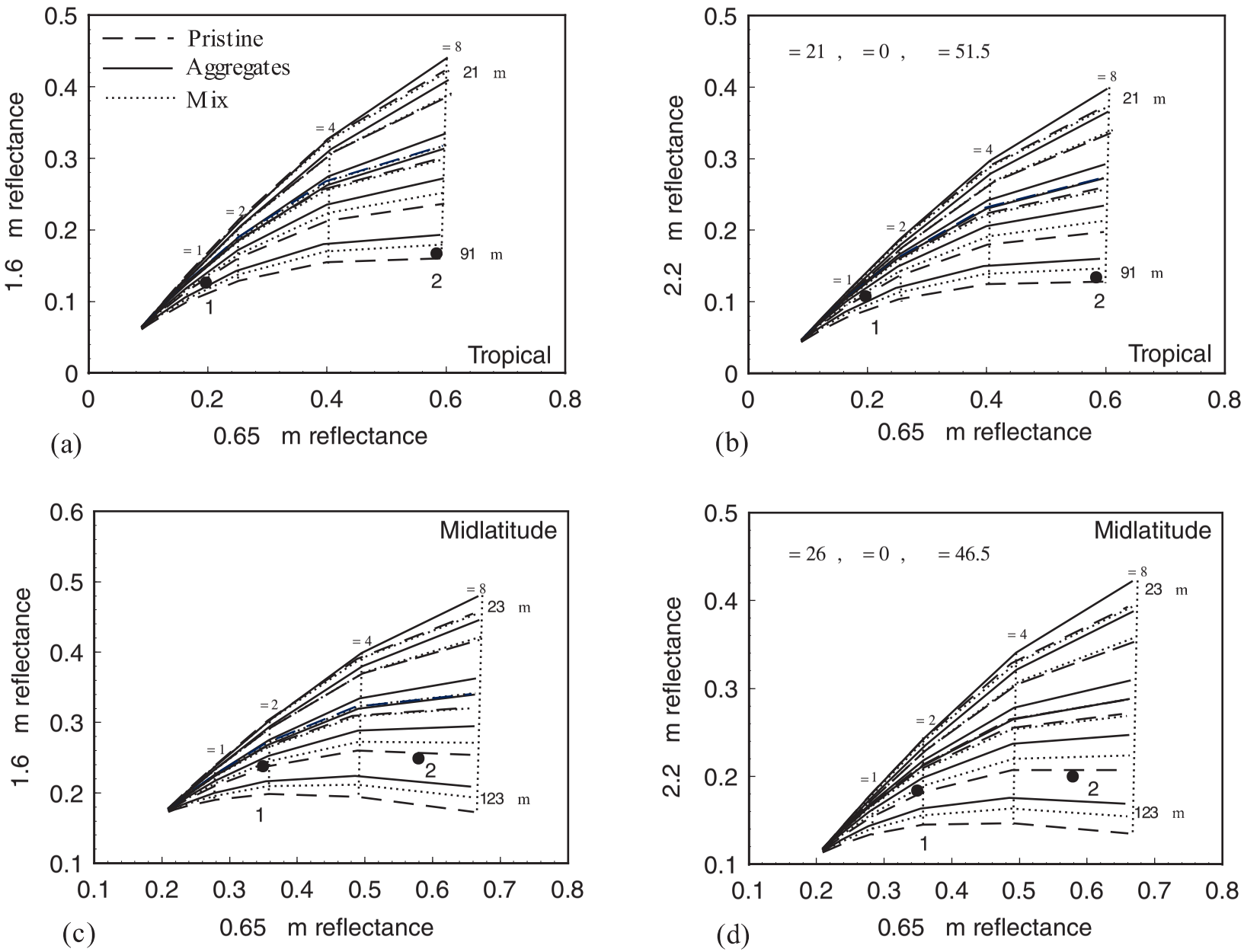
Pristine
Aggregates
Mix
Tropical
1.6 m reflectance
0.65 m reflectance
21 m
91 m
(a)
= 21 , = 0 , = 51.5
Tropical
2.2 m reflectance
0.65 m reflectance
21 m
91 m
(b)
Midlatitude
1.6 m reflectance
0.65 m reflectance
23 m
123 m
(c)
= 26 , = 0 , = 46.5
Midlatitude
2.2 m reflectance
0.65 m reflectance
23 m
123 m
(d)

Fig. 4

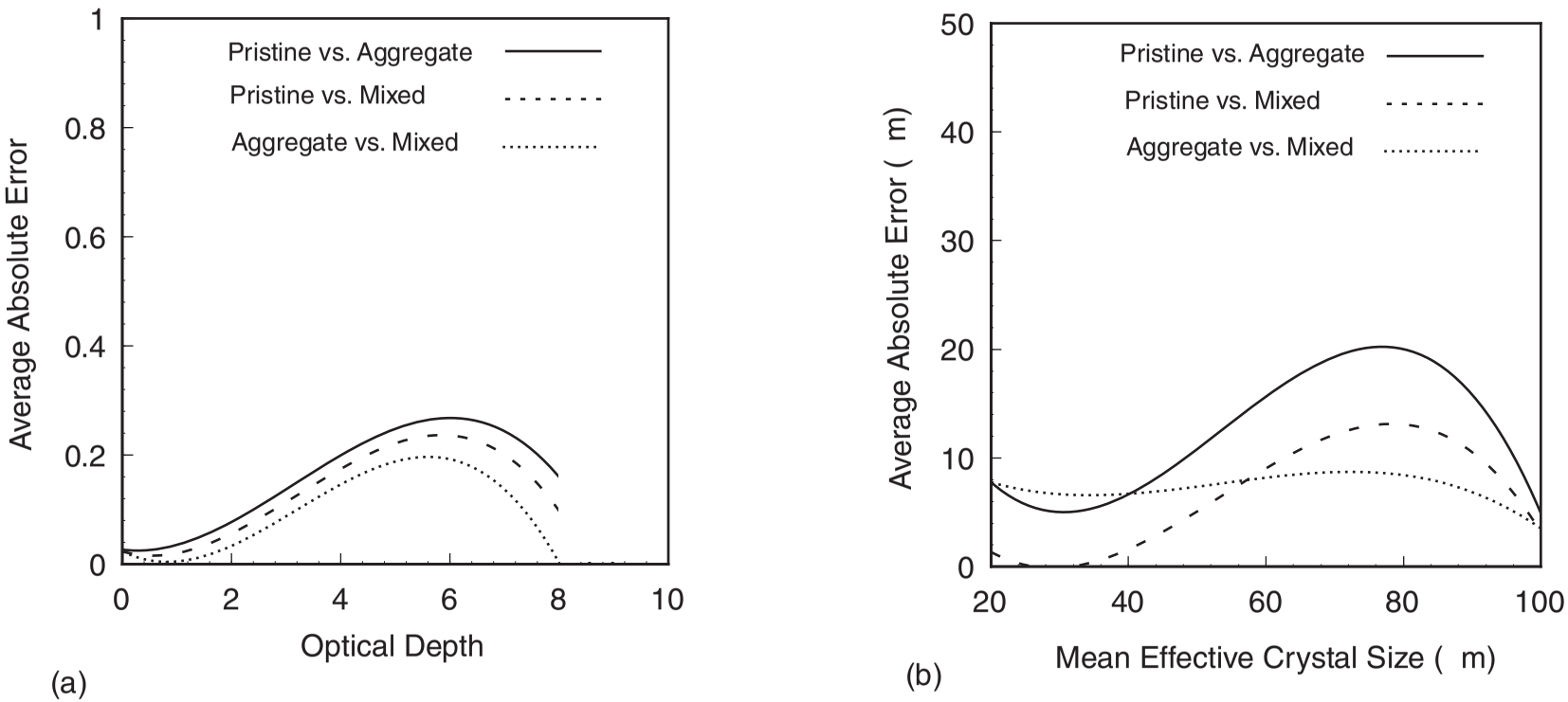
Pristine vs. Aggregate
Pristine vs. Mixed
Aggregate vs. Mixed
Average Absolute Error
Optical Depth
(a)
Pristine vs. Aggregate
Pristine vs. Mixed
Aggregate vs. Mixed
Average Absolute Error (m)
Mean Effective Crystal Size (m)
(b)

Fig. 5

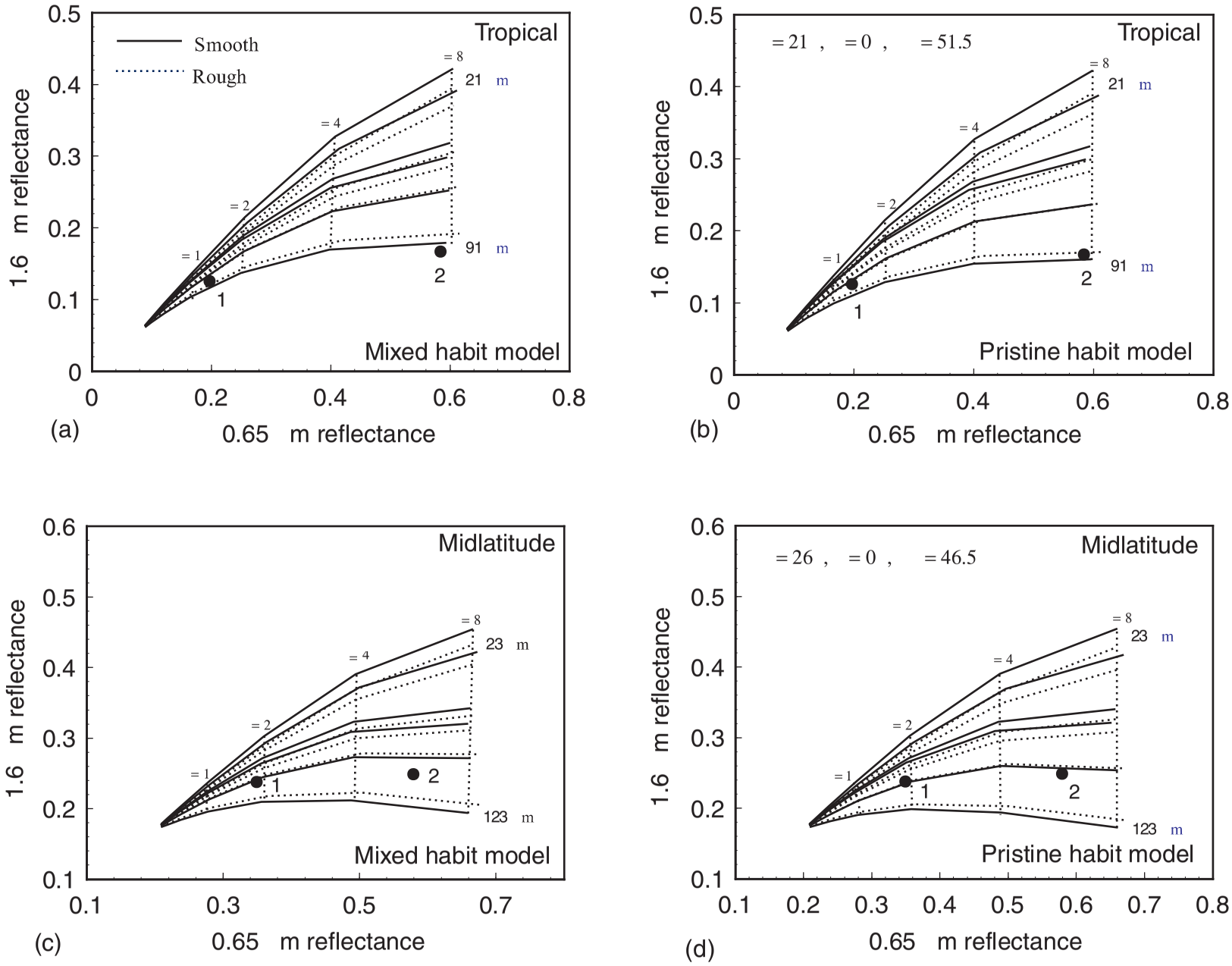
Tropical
Smooth
Rough
Mixed habit model
(a)
1.6 m reflectance
0.65 m reflectance
= 1
= 2
= 4
= 8
21 m
91 m
1
2
Tropical
= 21 , = 0 , = 51.5
Pristine habit model
(b)
Midlatitude
Mixed habit model
(c)
23 m
123 m
Midlatitude
= 26 , = 0 , = 46.5
Pristine habit model
(d)

Fig. 6

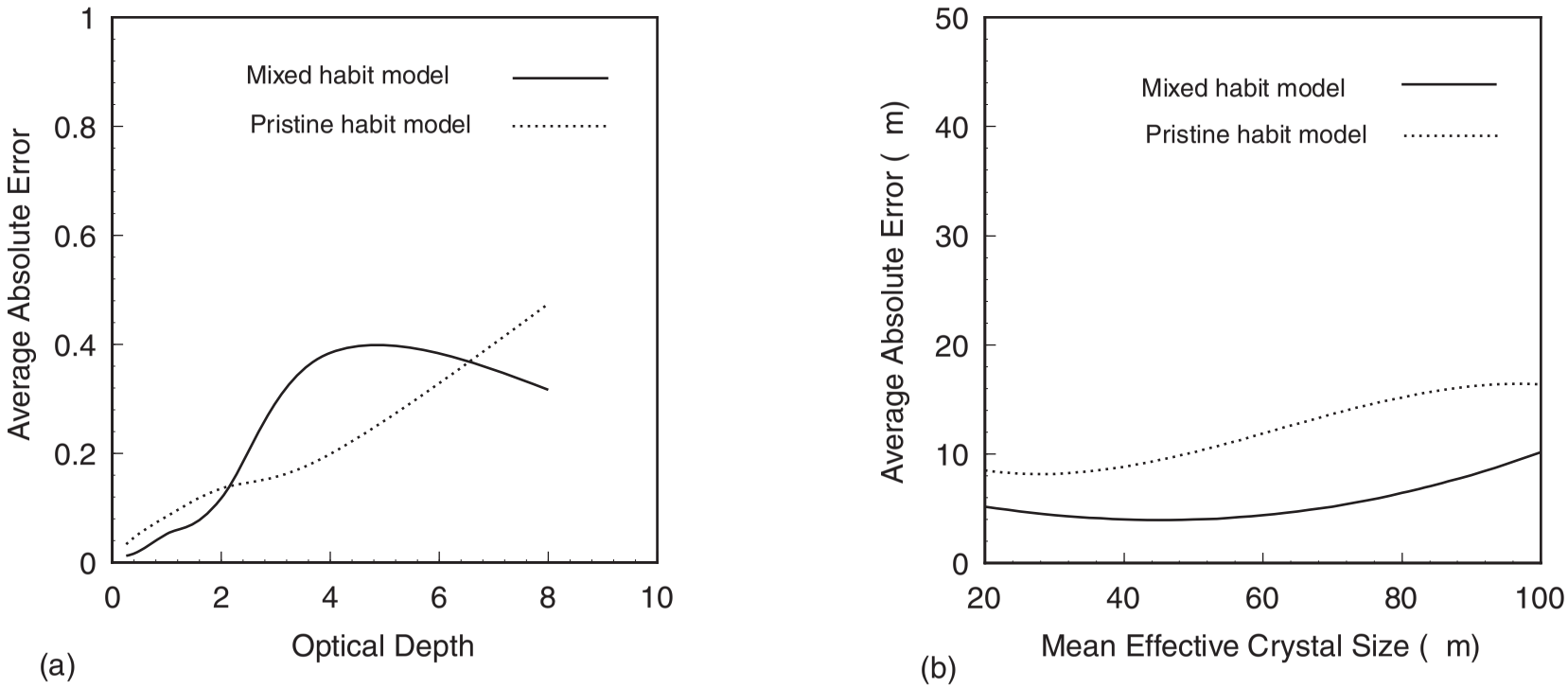
Mixed habit model
Pristine habit model
Average Absolute Error
Optical Depth
(a)
Mixed habit model
Pristine habit model
Average Absolute Error (m)
Mean Effective Crystal Size (m)
(b)

Fig. 7

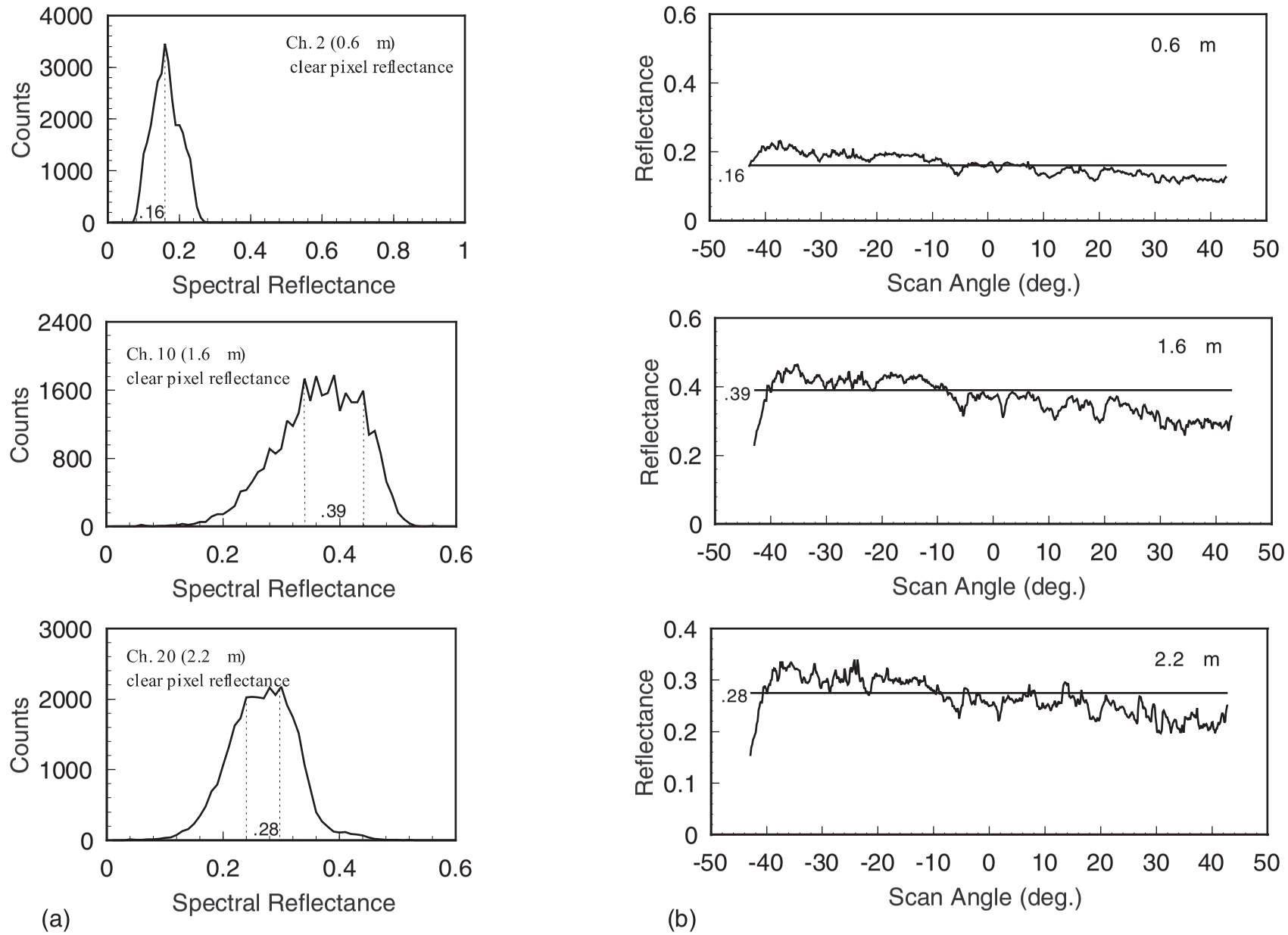
Ch. 2 (0.6 m)
clear pixel reflectance
Counts
Spectral Reflectance
.16
Ch. 10 (1.6 m)
clear pixel reflectance
.39
Ch. 20 (2.2 m)
clear pixel reflectance
.28
(a)
0.6 m
1.6 m
2.2 m
Reflectance
Scan Angle (deg.)
(b)

Fig. 8

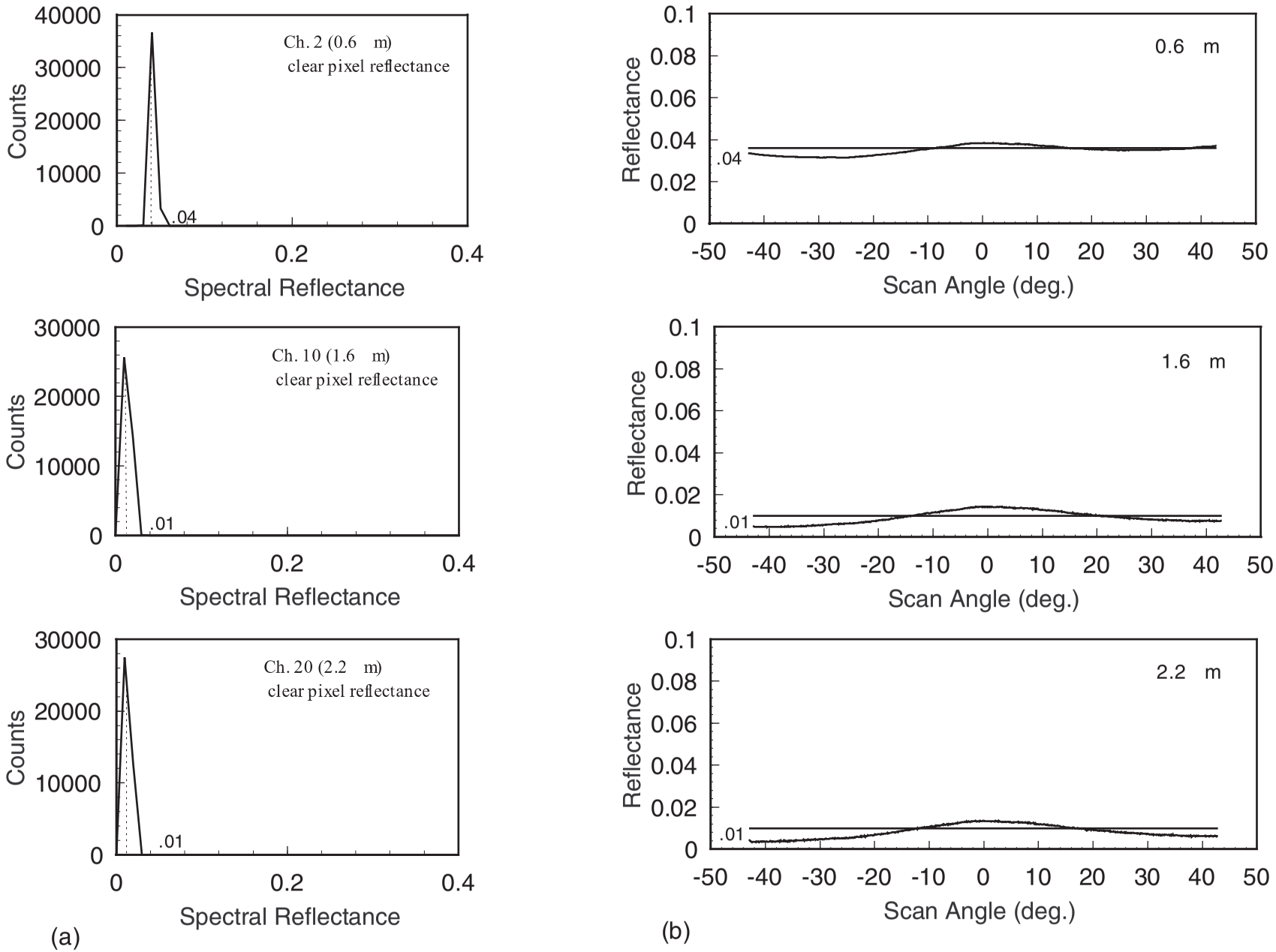
Ch. 2 (0.6 m)
clear pixel reflectance
Counts
Spectral Reflectance
.04
Ch. 10 (1.6 m)
clear pixel reflectance
.01
Ch. 20 (2.2 m)
clear pixel reflectance
.01
(a)
0.6 m
1.6 m
2.2 m
Reflectance
Scan Angle (deg.)
(b)

Fig. 9

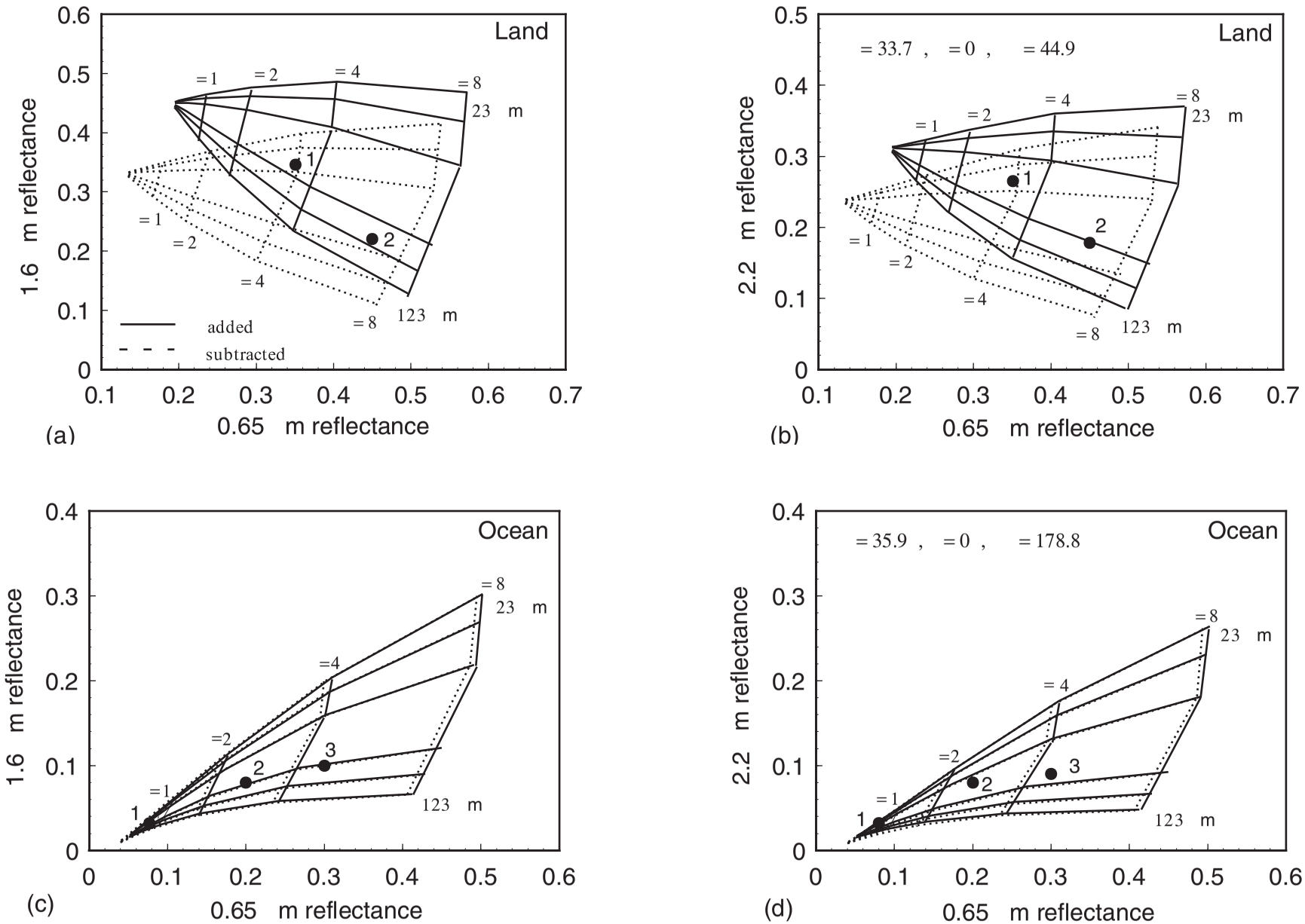
Land
= 1
= 2
= 4
= 8
23 m
123 m
added
subtracted
1.6 m reflectance
0.65 m reflectance
(a)
Land
= 33.7 , = 0 , = 44.9
2.2 m reflectance
0.65 m reflectance
(b)
Ocean
=1
=2
=4
=8
23 m
123 m
1.6 m reflectance
0.65 m reflectance
(c)
Ocean
= 35.9 , = 0 , = 178.8
2.2 m reflectance
0.65 m reflectance
(d)

Fig. 10

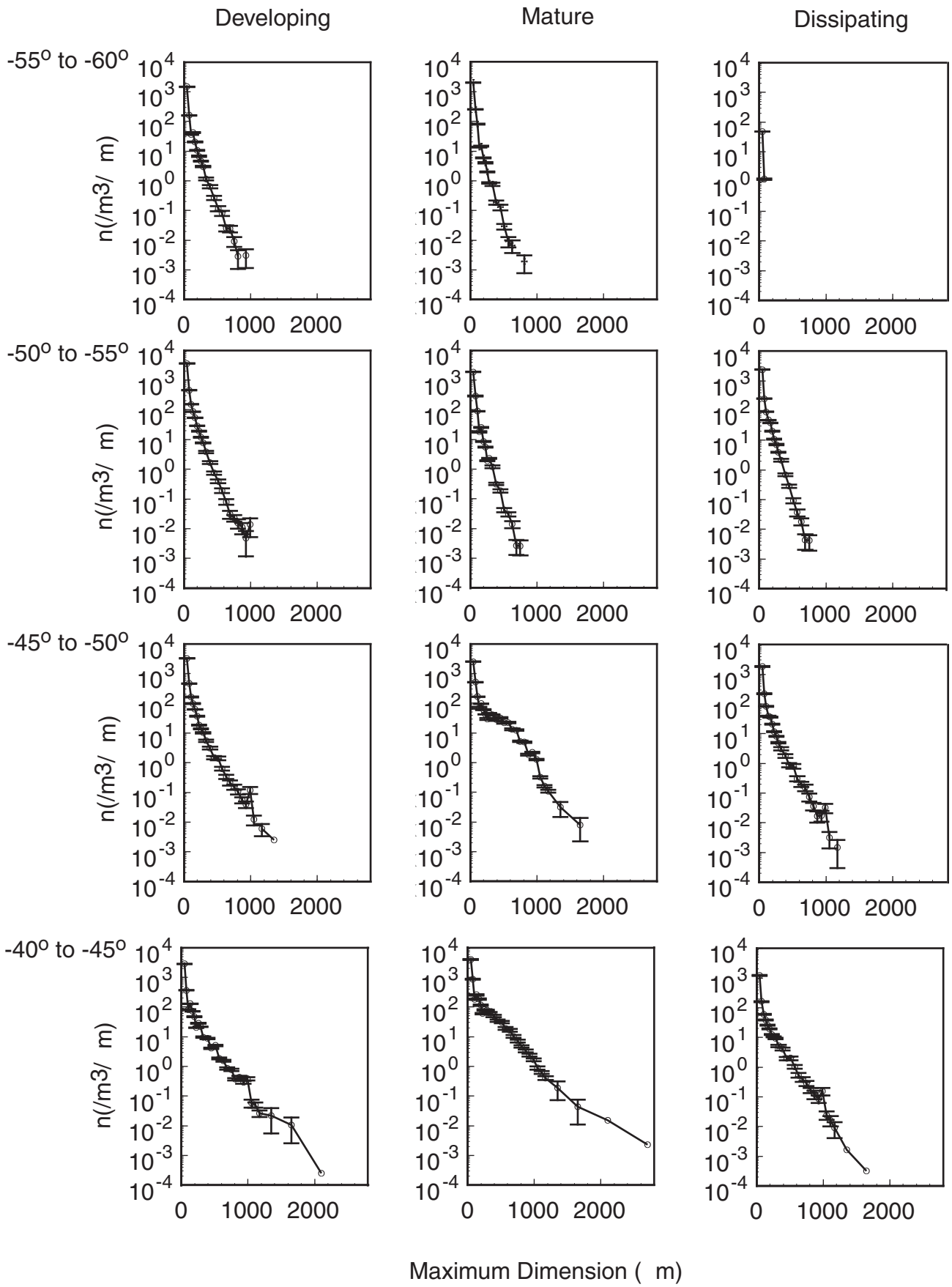
Developing
Mature
Dissipating
-55° to -60°
-50° to -55°
-45° to -50°
-40° to -45°
n(/m3/ m)
0
1000
2000
Maximum Dimension (m)

Fig. 11 (a)

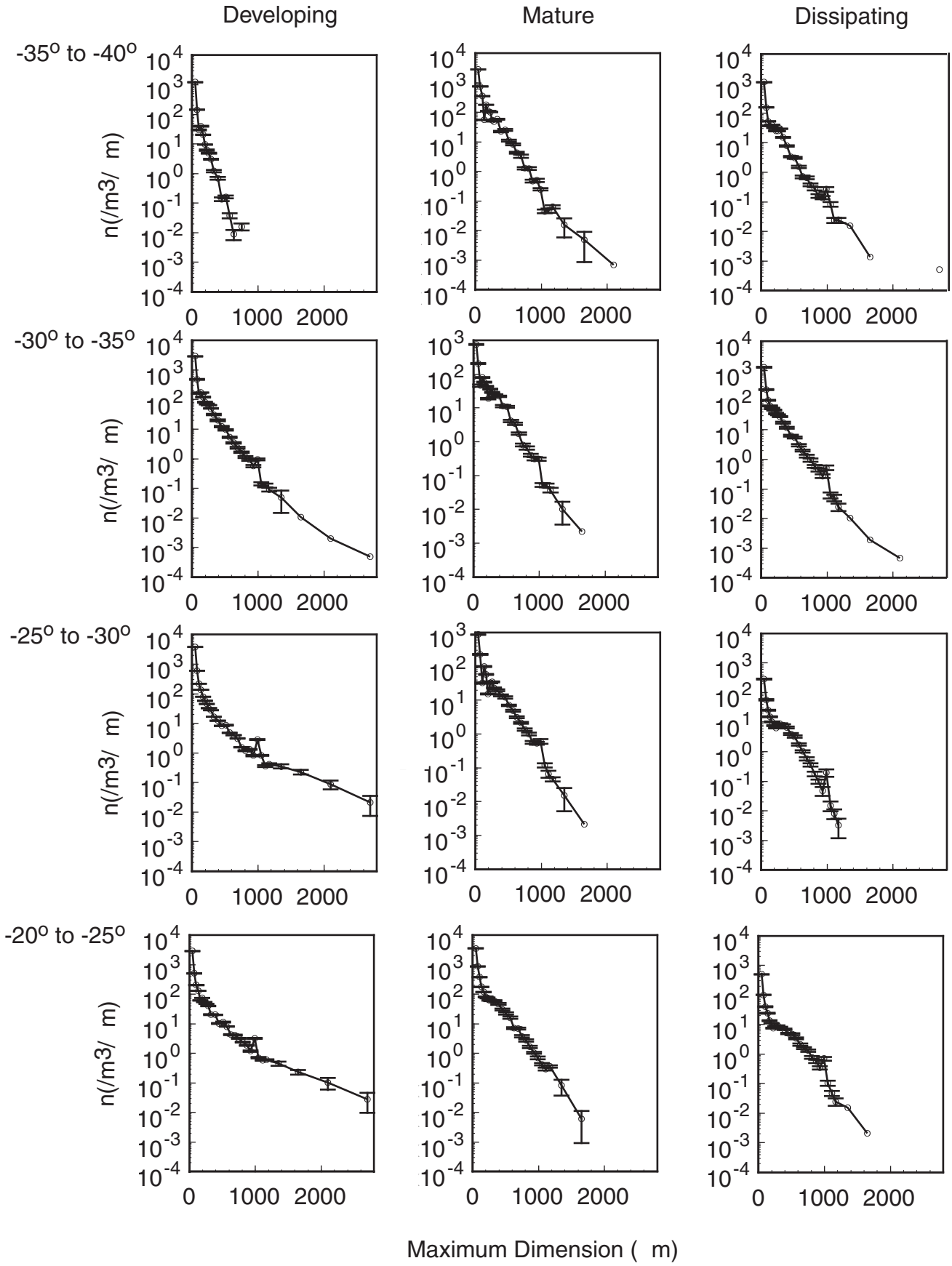
Developing
Mature
Dissipating
-35° to -40°
-30° to -35°
-25° to -30°
-20° to -25°
n(/m3/ m)
Maximum Dimension (m)

Fig. 11 (b)

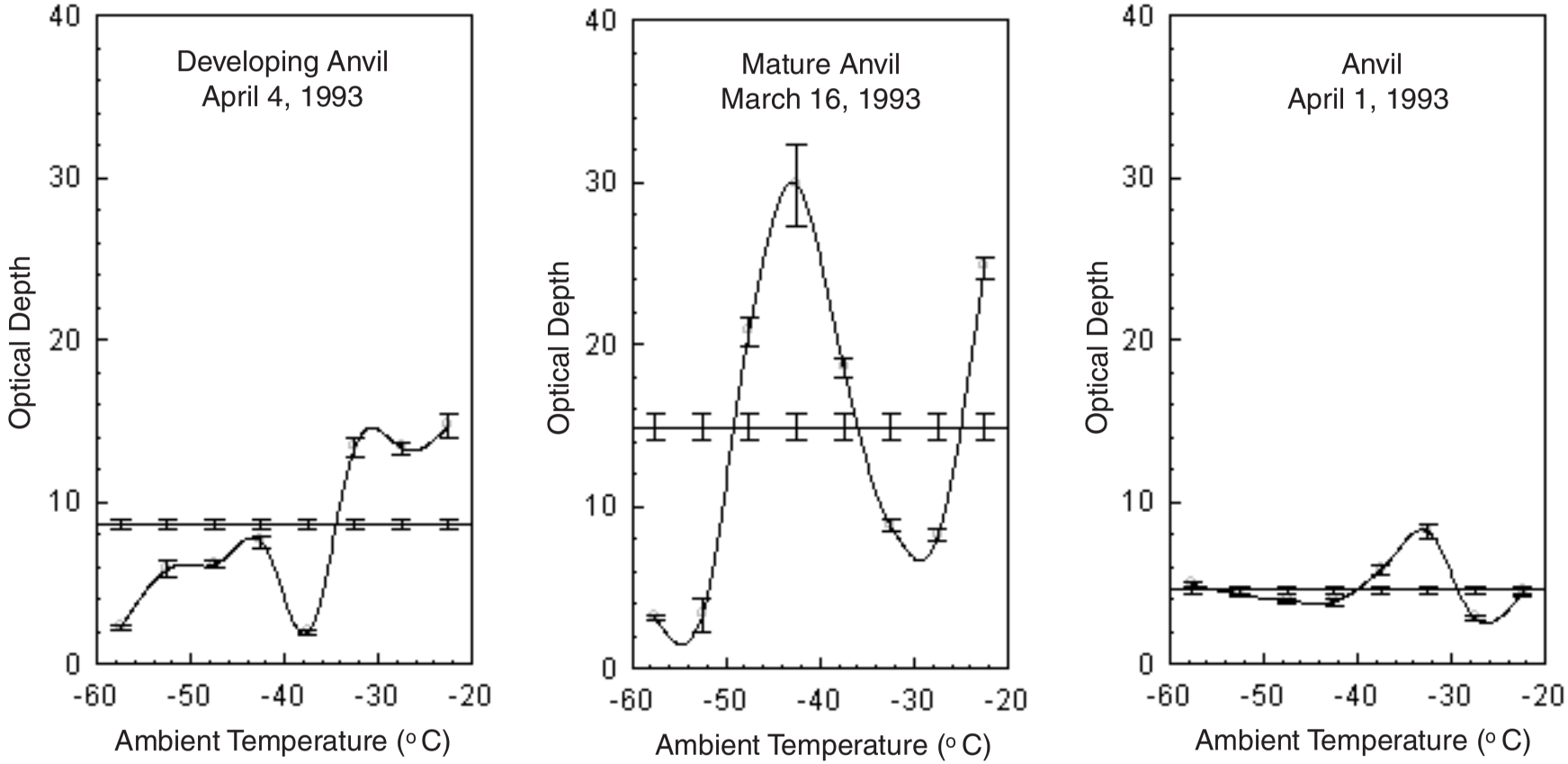
Developing Anvil
April 4, 1993
Mature Anvil
March 16, 1993
Anvil
April 1, 1993
Optical Depth
Ambient Temperature (° C)
0
10
20
30
40
-60
-50
-40
-30
-20

Fig. 12